Atmos. Chem. Phys., 26, 5407–5425, 2026
https://doi.org/10.5194/acp-26-5407-2026


Atmospheric Chemistry and Physics
Open Access
EGU

Research article

# The impact of aerosol-ice nuclei-cloud interactions on a typical spring dust-precipitation event in China

**Jian Zhang**[1,2], **Chunhong Zhou**[2], **Xiaoyu Shen**[2,3], **Hong Wang**[2,4], **Sunling Gong**[2,4,6,7], **and Xiaoye Zhang**[5]

[1]Key Laboratory for Aerosol-Cloud-Precipitation of China Meteorological Administration, Nanjing University of Information Science & Technology, Nanjing, Jiangsu, China
[2]Institute of Atmospheric Composition and Environmental Meteorology & Key Laboratory of Atmospheric Chemistry of CMA, Chinese Academy of Meteorological Sciences, Beijing, China
[3]Key Laboratory of Urban Air Particulate Pollution Prevention and Control of the Ministry of Ecology and Environment, College of Environmental Science and Engineering, Nankai University, Tianjin, China
[4]State Key Laboratory of Severe Weather, Chinese Academy of Meteorological Sciences, Beijing, China
[5]Laboratory of Climate Change Mitigation and Carbon Neutrality, Henan University, Zhengzhou, Henan, China
[6]National Observation and Research Station of Coastal Ecological Environments in Macao, Macao Environmental Research Institute, Macau University of Science and Technology, Macao, China
[7]Research Institute for Pollution and Carbon Mitigation Assessment, Tianfu Yongxing Laboratory, Chengdu, Sichuan, China

**Correspondence:** Chunhong Zhou (zhouch@cma.gov.cn) and Xiaoye Zhang (xiaoye@cma.gov.cn)

Received: 23 August 2025 – Discussion started: 9 September 2025
Revised: 9 March 2026 – Accepted: 9 March 2026 – Published: 22 April 2026

**Abstract.** To investigate the impact of ice nuclei (IN) activated by dust aerosols on precipitation over China, a new mechanism for online aerosol activation of IN has been embedded in the Global/Regional Assimilation and Prediction System-China Meteorological Administration Unified Atmospheric Chemistry Environment (GRAPES/CUACE). The original temperature-dependent IN nucleation scheme in the Double-Moment 6-Class (WDM6) has been improved by the new online aerosol–IN nucleation scheme, which is used to examine the effects of these processes during a typical dust-affected precipitation event in East Asia. Compared with the systematic underestimation in the original WDM6, the peak values of nucleated INs reach $10^{-4}$ $L^{-1}$ with the improved scheme, which is closer to observations. Above 7 km, dust suppresses both heterogeneous nucleation and deposition growth. Thus, the total production rate of cloud ice drops to less than 24 % of that in the control test T_CTL, promoting snow formation and reducing the total ice-phase hydrometeor content to 70 %–85 % of T_CTL. Between 4 and 7 km, dust enhances heterogeneous nucleation of cloud ice but suppresses deposition growth, thereby reducing the total ice-phase hydrometeor content to 85 %–91 % of T_CTL. Below 4 km, dust suppresses the conversion of water vapour to cloud water, thereby reducing the liquid-phase hydrometeor content to 90 %–95 % of T_CTL. Dust can also modify the precipitation distribution, bringing it closer to observations. It suppresses precipitation near dust source areas, where mean precipitation decreases by about 4.5 mm, while the downstream event-mean precipitation increases by about 1.1 mm.

Published by Copernicus Publications on behalf of the European Geosciences Union.

## 1 Introduction

The formation of cloud ice is one of the key processes in ice-phase precipitation, and ice nuclei (IN) associated with aerosols play a crucial role in the development of cloud ice, particularly in mid- to high-latitude areas and in the upper troposphere (Li et al., 2022; Chen et al., 2023; Knopf and Alpert, 2023). This is because homogeneous nucleation without IN occurs only below −40 °C, which is relatively rare in natural atmospheric environments (Eastwood et al., 2008; Herbert et al., 2015; Kumar et al., 2020; Che et al., 2021). In contrast, heterogeneous nucleation mediated by IN can occur under ice-supersaturated conditions at much higher temperatures, making it the dominant pathway for cloud ice formation.

Aerosols can serve as IN, participating in cloud formation, altering cloud microphysical properties and lifetimes, and thereby affecting precipitation (Albrecht, 1989; Andreae and Crutzen, 1997). Among different species, mineral dust is recognized as one of the primary sources of atmospheric IN (Khain et al., 2000; Nenes et al., 2014; Tobo et al., 2019). Dust particles have unique surface structures that facilitate the adsorption and binding of water molecules, promoting the formation of cloud ice (Possner et al., 2017; Stevens et al., 2018). Stith et al. (2009) and DeMott et al. (2015) have found a strong correlation between IN number concentration and aerosols with diameters larger than 0.5 µm, with mineral dust accounting for 33 %–50 % of the total IN. Jiang et al. (2016) combined IN measurements during dust conditions at multiple sites in China, including Xinjiang (Jiang et al., 2016), Mt. Huangshan (Jiang et al., 2015), and Nanjing (Yang et al., 2013), and found that IN concentrations were significantly higher than those under non-dust conditions. Tobo et al. (2020) observed that IN concentrations increased markedly during dust events in Tokyo when temperatures exceeded −25 °C. In addition, the increased solubility of aged dust aerosol enhances its ability to act as cloud condensation nuclei (CCN), thereby further influencing precipitation (Trochkine et al., 2003).

Compared with the relatively well-understood impacts of aerosols as CCN, the role of dust as IN is considerably more complex and remains poorly understood, with substantial uncertainties (Kaufman et al., 2002; Eastwood et al., 2008; Pan et al., 2017; Possner et al., 2017). Based on the chemistry (WRF-Chem) model and multiple observational and reanalysis data, Wang et al. (2024) found that dust aerosols can suppress light precipitation by increasing atmospheric stability and inhibiting the conversion of cloud droplets into raindrops. In contrast, Naeger (2018) found that dust could enhance precipitation over Florida based on multi-sensor satellite observations and field campaigns. More recently, Hu et al. (2023) demonstrated that the impact of springtime dust on precipitation is strongly modulated by the presence of other aerosol types. Liu et al. (2024) analysed the spatiotemporal patterns and trends of dust aerosols and precipitation and found that increased dust suppresses precipitation over source regions such as the Gobi and Taklamakan deserts, but enhances precipitation in downwind areas such as northern China. Overall, because multiple factors influence precipitation beyond aerosols, it remains challenging to quantify the impact of dust on precipitation from observations alone (Zhou et al., 2016; Stier et al., 2024), highlighting the need for process-oriented numerical modelling studies with physically based aerosol–ice nucleation parameterisations.

A numerical model is a crucial approach for numerically studying the impact of dust on precipitation. In early cloud microphysics schemes, the ice nucleation scheme did not account for aerosols, with IN concentrations typically expressed as functions of temperature or supersaturation (DeMott et al., 2010). Moreover, many cloud ice microphysical schemes were single-moment, which only simulated the mass mixing ratio of cloud ice. Such single-moment schemes often led to large biases in cloud ice mass concentrations (Molthan and Colle, 2012; Igel et al., 2015). In contrast, double-moment ice schemes, which simulate both cloud ice mass and number concentrations, outperform single-moment schemes in simulating structure, life cycle, cloud coverage, precipitation, and microphysical properties (Pu and Lin, 2015; Zhao et al., 2021). The double-moment ice schemes can provide more stable and improved precipitation simulations (Kang et al., 2018; Shen et al., 2022, 2024). Mascioli et al. (2021) used the Thompson aerosol-aware microphysics scheme, incorporating the IN nucleation scheme of DeMott et al. (2010), to study the sensitivity of precipitation to different prescribed dust aerosol concentrations. Park and Lim (2023) developed the revised Weather Research and Forecasting Double-Moment 6-class (WDM6) scheme by implementing prognostic cloud ice number concentrations. The excess generation of cloud ice mixing ratio is considerably alleviated. However, these studies did not establish an explicit quantitative relationship between online aerosols and IN. Su and Fung (2018a) implemented the simplified Goddard Chemistry Aerosol Radiation and Transport aerosol model (GOCART) together with Shao's dust emission scheme (Kang et al., 2011; Shao et al., 2011) in WRF/Chem and incorporated the online IN nucleation scheme of DeMott et al. (2015) for producing real-time IN into the double-moment Thompson–Eidhammer microphysics scheme. They analysed the impact of dust on radiative forcing and temperature in East Asia, but only the sensitive impacts on precipitation rates in March and April 2012 (Su and Fung, 2018b). The spring of 2012 was not a typical dust season; most dust storms concentrated in Mongolia. Therefore, the microphysical pathways through which dust affects precipitation during typical dust events remain insufficiently studied. In this study, we focus on a representative spring dust precipitation event and explicitly examine the cloud microphysical processes associated with dust-induced heterogeneous ice nucleation, together with direct comparisons to precipitation observations in the Global/Regional

Assimilation and PrEdiction System, China Meteorological Administration (CMA) Unified Atmospheric Chemistry Environment (GRAPES/CUACE) model. GRAPES/CUACE provides online sectional aerosol concentrations with multi-chemical composition information (Wang et al., 2010; Zhou et al., 2012). Zhou et al. (2016) introduced an online aerosol–CCN–cloud interaction scheme into the system, allowing the model to simulate real-time CCN activation and their influence on precipitation. However, in the GRAPES/CUACE microphysics scheme WDM6, IN is a function of temperature only, and cloud ice is represented by a single-moment scheme only for the mass mixing ratio (Hong et al., 2004; Zhang et al., 2022).

To address these limitations, this study implements a double-moment cloud ice scheme and incorporates an online aerosol–IN nucleation scheme to explicitly represent heterogeneous processes. Using this improved framework, we then investigate the impact of dust on precipitation through a typical dust-affected precipitation event in East Asia. This paper is organised as follows: Sect. 2 introduces the model configuration, cloud microphysical processes, the online aerosol–IN nucleation scheme, the study region, and the observational datasets. Section 3 presents the evaluation of the improved model's simulation performance and discusses the effects of dust on precipitation. Section 4 summarises the main conclusions of the study.

## 2 Model description and methodology

### 2.1 GRAPES/CUACE

The GRAPES is a fully compressible, non-hydrostatic numerical weather model that employs a semi-implicit, semi-Lagrangian discretisation scheme (Chen et al., 2008; Xu et al., 2008; Zhang and Shen, 2008; Wang et al., 2022). Its physical parameterisation packages include cumulus convection, single-moment cloud microphysics, radiation, land surface processes, and boundary layer processes. CUACE is a regional chemical weather forecasting system developed by Gong and Zhang (2008), coupled online with GRAPES (Wang et al., 2010). It is capable of simulating seven aerosol species of sulfate, nitrate, ammonium, black carbon, organic carbon, sea salt, and dust (Zhou et al., 2008, 2012; Wang et al., 2015). The sectional dust emission scheme is by Marticorena and Bergametti (1995) and Alfaro and Gomes (2001), which has been improved by surface dust flux observations and desertification in East Asia (Gong et al., 2003), and a new desertification map and soil texture samples from Chinese deserts (Zhou et al., 2019, 2024). The aerosol size spectra have been divided into 12 size bins with a radius range of 0.005–0.01, 0.01–0.02, 0.02–0.04, 0.04–0.08, 0.08–0.16, 0.16–0.32, 0.32–0.64, 0.64–1.28, 1.28–2.56, 2.56–5.12, 5.12–10.24, and 10.24–20.48 µm. GRAPES/CUACE has a horizontal resolution of 0.15° and 31 vertical levels extending to approximately 28.6 km.

### 2.2 WDM6 microphysics scheme

In this study, we select the WDM6 microphysics scheme in GRAPES to simulate precipitation (Hong et al., 2004; Zhang et al., 2022). The WDM6 scheme simulates the mass mixing ratio of water vapour (Qv), as well as the mass and number concentrations of cloud water (Qc) and rainwater (Qr) in warm clouds. For icy clouds, it includes the mass mixing ratios of cloud ice (Qi), snow (Qs), and graupel (Qg). A double-moment cloud ice scheme by Park and Lim (2023) is incorporated into the WDM6 scheme, enabling explicit prediction of cloud ice number concentration. A sectional CCN-activated scheme has been introduced in WDM6 in GRAPES/CUACE, connecting the multi-component, multi-section aerosols from CUACE to the WDM6 microphysics and the sub-grid convective parameterisation scheme via newly activated CCN at each time step (Zhou et al., 2016).

### 2.3 Online aerosol-IN nucleation scheme

In the original WDM6 scheme, when the temperature is below 0 °C, the increase in cloud ice mass concentration arises from two processes: heterogeneous nucleation (Pigen) and deposition–sublimation of cloud ice (Pidep, when positive). Both consume water vapour to form ice clouds. The abbreviations for the remaining cloud microphysical processes are listed in Table 2. The IN concentration, Nice ($m^{-3}$), is calculated by a classical ice nuclei nucleation scheme, which is an empirical function of temperature and does not account for the influence of atmospheric aerosols (Hong et al., 2004):

$$\text{Nice} = 10^3 e^{0.1(T_0 - T_k)} \quad (1)$$

Where, $T_k$ is atmospheric temperature, $T_0$ is the freezing point (273.15 K).

This study implements an online aerosol-IN nucleation scheme in GRAPES/CUACE that accounts for heterogeneous ice nucleation processes influenced by atmospheric aerosols. Heterogeneous nucleation mechanisms are generally classified into immersion freezing, condensation freezing, deposition nucleation, and contact freezing (Hiranuma et al., 2015; Ilotoviz et al., 2016; Lee et al., 2017). Among these mechanisms, immersion freezing, condensation freezing, and deposition nucleation are selected, as they are relatively well developed. This selection is based on the fact that dust aerosols primarily affect ice nucleation at temperatures below 258.15 K through these three mechanisms (Cantrell et al., 2013; Patnaude et al., 2025), whereas the efficiency of contact freezing by dust particles is relatively low (Niehaus et al., 2014).

Immersion freezing is a heterogeneous ice nucleation process with the existence of liquid drops at temperatures between 233.15 and 273.15 K, in which an ice nucleus is immersed in a supercooled droplet, thereby triggering freezing into an ice crystal (Boose et al., 2016). Immersion freezing consumes water vapour to form cloud ice. The initial

size of the ice crystal is influenced by the size of the liquid droplet (Fan et al., 2014; Gibbons et al., 2018), therefore the cloud ice formation through this mechanism is relatively easier compared to other nucleation mechanisms. The selected DeMott et al. (2015),immersion-freezing nucleation scheme here is developed by DeMott et al. (2015) and is based on continuous-flow diffusion-chamber measurements. The number concentration of ice nuclei, Nicenui ($m^{-3}$), activated via immersion freezing is given by:

$$\text{Nicenui} = 3 \cdot n_{\text{aer},0.5}^{1.25} \cdot e^{(0.46 \cdot (273.16 - T_k) - 11.6)} \quad (2)$$

Where, $n_{\text{aer},0.5}^{1.25}$ is the number concentration of insoluble aerosol particles with diameters exceeding 0.5 µm, such as dust, black carbon and part of organic carbon.

Deposition and condensation freezing are both heterogeneous ice nucleation processes that occur at temperatures between 248.15 and 258.15 K (Chen et al., 2019). In condensation freezing, water vapour first condenses on the surface of IN and subsequently freezes to form an ice crystal, while in deposition nucleation, water vapour directly deposits onto the IN surface (Kanji et al., 2017). The ice formation through these two pathways is generally harder than that through immersion freezing (DeMott et al., 2015). The parameterisation used here follows the formulation of Chen et al. (2019). In Jiang et al. (2016), the ice-nucleating ability of dust aerosols was derived from measurements conducted at several sites in China (Yang et al., 2013; Jiang et al., 2015, 2016), using a static vacuum vapour diffusion chamber based on the FRIDGE (Frankfurt Ice Nuclei Deposition Freezing Experiment) design. Chen et al. (2019) further refined the parameterisation to explicitly represent deposition and condensation freezing processes within a specified temperature range. The number concentration of ice nuclei produced by deposition and condensation freezing, Nicenud ($m^{-3}$), is calculated as follows:

$$\text{Nicenud} = 5.7 \times 10^{-7} n_{\text{aer},0.5}^{0.018(273.16 - Tk) - 0.007 S_i + 0.342} \cdot (273.16 - Tk)^{3.745} \cdot S_i^{1.31} \quad (3)$$

Where, $S_i$ is supersaturation with respect to ice.

WDM6 uses the formula $\rho q_{I0}$ ($\text{kg m}^{-3}$) $= 4.92 \times 10^{-11} N_{\text{ice}}^{1.33}$ and Pigen ($\text{kg kg}^{-1}\ \text{s}^{-1}$) $= \frac{(q_{I0} - q_I)}{\Delta t}$ to calculate newly nucleation of ice. Where, $\rho$ denotes the newly-formed air density, and $q_{I0}$ is the predicted ice mixing ratio ($\text{kg kg}^{-1}$). $\Delta t$ is the integration time step. Production rate for heterogeneous nucleation is calculated as the difference between $q_{I0}$ and the current ice mixing ratio ($q_I$). However, it does not account for the influence of nucleated IN size or the specific characteristics of different heterogeneous ice nucleation mechanisms on ice crystal development.

Here, the mass production rate of cloud ice newly nucleated is calculated as follows:

$$\text{Pinud} = 4/3\pi \frac{\rho_i}{\rho_a} \left( r_{\text{df}}^3 N_{\text{icenud}} \right) / \Delta t$$
$$\text{Pinui} = 4/3\pi \frac{\rho_i}{\rho_a} \left( r_{\text{if}}^3 N_{\text{icenui}} \right) / \Delta t \quad (4)$$

Where, Pinud ($\text{kg kg}^{-1}\ \text{s}^{-1}$) is the mass production rate for deposition/condensation freezing, Pinui ($\text{kg kg}^{-1}\ \text{s}^{-1}$) is for immersion freezing. Pinud depletes water vapour to form cloud ice, while Pinui depletes cloud water to form cloud ice. $\rho_i$ is 500 $\text{kg m}^{-3}$ (Park and Lim, 2023). $r_{\text{if}}$ represents the initial radius of cloud ice formed via immersion freezing, while $r_{\text{df}}$ represents the initial radius of cloud ice formed through deposition and condensation freezing, respectively. $\Delta t$ is the integration time step. In the new online scheme, the production rate for nucleated IN number concentration (Nigen) is the sum of Nicenui and Nicenud.

The typical range of ice crystal radius in East Asia is about 10–100 µm (Chen et al., 2021), droplet radius range is about 1–30 µm (Um et al., 2018; Yang et al., 2021). Considering ice crystals generally grow from smaller particles and the radius of initial ice crystal size are often smaller than observed values, and with reference to the bin sizes of aerosol particles in CUACE (Um et al., 2018; Chen et al., 2021; Yang et al., 2021), this study assumes the characteristic radius of ice crystals of $r_{\text{df}}$ and $r_{\text{if}}$ to be:

$$\begin{cases} r_{\text{df}} = 10\,\mu\text{m} (\text{r}_{\text{aer}} < 10\,\mu\text{m}) \\ \text{r}_{\text{df}} = 30\,\mu\text{m} (r_{\text{aer}} > 10\,\mu\text{m}) \end{cases}$$
$$\begin{cases} r_{\text{if}} = 30\,\mu\text{m} (r_{\text{aer}} < 10\,\mu\text{m}) \\ r_{\text{if}} = 50\,\mu\text{m} (r_{\text{aer}} > 10\,\mu\text{m}) \end{cases} \quad (5)$$

Then, the original production rate for nucleation of ice from vapour Pigen in WDM6 is replaced by the Pinud and Pinui described above.

## 2.4 Case description and test design

The typical dust-affected precipitation event

The typical dust-affected precipitation event spans from 00:00 UTC on 9 April to 00:00 UTC on 15 April 2018 and includes two dust storm events in East Asia. One is from 9 to 11 April, originating in Mongolia and affecting northern China. Numerous dust storm phenomena are observed in Mongolia, while blowing and floating dust phenomena are reported in central and western Inner Mongolia, central Gansu, Ningxia, northern Shaanxi, most parts of Shanxi, southern Hebei, northern Henan, and western Shandong in China (see Fig. S1 in the Supplement for locations). Another event is from 13 to 14 April. It also gains with widespread dust storms in Mongolia and central Inner Mongolia, and with blowing or floating dust observed in central Inner Mongolia, northern Shanxi, Beijing, Tianjin, and northern Hebei in China. Between the two dust storm events, the precipitation occurred from west to east, covering most of northern

**Table 1.** Tests designed for different types of microphysics scheme.

| Test | Warm cloud | Cold cloud |
|---|---|---|
| T_CTL | online aerosol–CCN interaction scheme | original WDM6 |
| T_IN | online aerosol–CCN interaction scheme | online aerosol-IN nucleation scheme |

China extending to the Yangtze River area, from 00:00 UTC on 12 April to 00:00 UTC on 15 April, concentrated in Shaanxi, Henan, southern Hebei, and along the Yangtze River in Sichuan, Hubei, Anhui, and the Jiangsu-Zhejiang-Shanghai area.

Figure 1a presents the dust-affected areas by dust phenomenon from Meteorological stations and $PM_{10}$ from the National Environmental Monitoring Network of the Ministry of Environmental Protection. Based on the distribution of dust in this event, the domain bounded by 90–135° E and 20–54° N is defined as the major dust-affected area (DA, region 1 in Fig. 1). Together with the real precipitation distribution (Fig. 5a), the domain bounded by 103–130.5° E and 27.5–50° N is defined as the dust-affected precipitation (DP) area (DPA, region 2 in Fig. 1). The whole model domain covers 70–145° E and 15–64.5° N, containing the DA and DPA. To investigate the impact of dust on precipitation in regions distant from the dust source in Sect. 3.3, we calculate horizontal hydrometeor fluxes across 116° E (33–50° N) and 33° N (103–116° E) during 12:00 UTC on 12 April to 18:00 UTC on 13 April (Fig. 6). The area bounded by 103–116° E and 33–50° N is defined as the near-dust-source area (NDSA, region 3 in Fig. 1).

GRAPES/CUACE successfully reproduces both the spatial distribution and intensity of the dust events (Fig. 1b). Considering that many radar observations and model studies have indicated that dust mainly participates in heterogeneous ice nucleation as ice nuclei within the mid-tropospheric layer (−20–0°) (Haarig et al., 2019; He et al., 2021, 2023), which corresponds to altitudes between 4 and 7 km in the present case, Fig. 1c shows the simulated dust concentration within this layer.

### Test design

As shown in Table 1, two tests are designed. The first test uses the online aerosol–CCN–cloud interaction scheme from Zhou et al. (2016), denoted as T_CTL. Based on T_CTL, the second test adds the online aerosol-IN nucleation scheme described in Sect. 2.3, denoted as T_IN.

The successive integration is divided into several three-day intervals, with a warm restart between them. It starts at 00:00 UTC on 5 April 2018, with 6 d spinning up for tracers in CUACE. As simulation time increases, integration errors tend to accumulate (Zhang et al., 2019), and to minimise the influence of initial conditions on precipitation, the simulations in this study were divided into several time segments: 5–8, 8–11, 11–14, and 13–16 April. Among these, the simulation results for 13 April were taken from the 11–14 April experiment to minimise the influence of initial conditions on precipitation development. Except for water vapour, all initial hydrometeor values are zero for each run. The model outputs 1-hourly precipitation data. To compare with the observed 6-hourly precipitation, the model outputs are temporally interpolated to the observation timestamps.

The initial and boundary meteorological conditions for GRAPES/CUACE are from the Final Operational Global Analysis data produced jointly by the National Centers for Environmental Prediction (NCEP) and the National Center for Atmospheric Research (NCAR) at a temporal resolution of 6 h and a spatial resolution of 0.25°. The anthropogenic emissions are from the Multi-resolution Emission Inventory for China (Li et al., 2017).

### 2.5 Data and evaluation methodology

The initial and boundary meteorological conditions for GRAPES/CUACE are obtained from the NCEP/NCAR Final Operational Global Analysis (FNL) data, with a temporal resolution of 6 hours and a spatial resolution of 0.25°. Dust observations are obtained from two sources: weather phenomena from the CMA surface meteorological observation network with a 3-hour temporal resolution, and $PM_{10}$ and $PM_{2.5}$ concentration data from the national environmental monitoring network of the Ministry of Ecology and Environment of China with a 1-hour temporal resolution. 6-hour rainfall data are also from the CMA surface meteorological observation network. As there are more than 2000 precipitation stations in DA, only 63 level-1 and level-2 stations are selected for evaluation, of which 43 are in DPA to avoid overfitting in the model outputs. Due to the complex sources of $PM_{10}$ and considering the relatively long atmospheric residence time of dust, we select precipitation stations where the $PM_{2.5}/PM_{10}$ ratio is less than 0.6 within 24 h prior to the precipitation event as representative of dust-influenced precipitation (DP) stations (Wang and Yan, 2007; Filonchyk et al., 2019).

Model performance is evaluated using mean absolute error (MAE), root mean square error (RMSE), and symmetric mean absolute percentage error (sMAPE) (Harmoko et al., 2025):

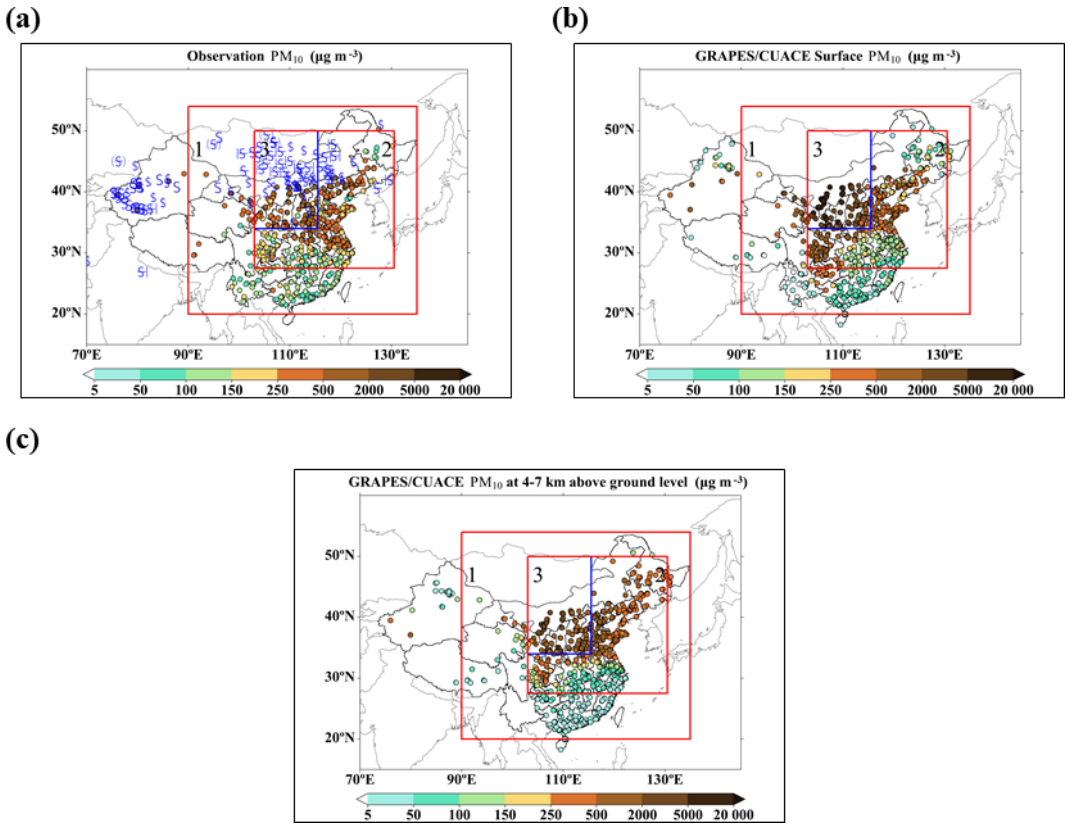


**Figure 1.** Observed and simulated affected areas of the dust events from 11 to 15 April (region 1 is DA; region 2 is DPA; region 3 is NDSA). **(a)** Observed distribution of most sever dusty weather phenomena and maximum $PM_{10}$ concentration for each station during the test time; **(b)** Same as **(a)** but for maximum $PM_{10}$ concentration by GRAPES/CUACE; **(c)** Maximum $PM_{10}$ concentration distribution in the layer of 4–7 km in height by GRAPES/CUACE.

$$\mathrm{MAE} = \frac{\sum_{i=1}^{n} |r_{\mathrm{mi}} - r_{\mathrm{oi}}|}{n}$$

$$\mathrm{RMSE} = \sqrt{\frac{\sum_{i=1}^{n} (r_{\mathrm{mi}} - r_{\mathrm{oi}})^2}{\mathrm{n}}}$$

$$\mathrm{sMAPE} = \frac{1}{n} \sum_{i=1}^{n} \frac{|r_{\mathrm{mi}} - r_{\mathrm{oi}}|}{|r_{\mathrm{mi}}| + |r_{\mathrm{oi}}|}$$

$$\mathrm{aMAPE} = \frac{r_{\mathrm{mi}} - r_{\mathrm{oi}}}{|r_{\mathrm{mi}}| + |r_{\mathrm{oi}}|} \quad (6)$$

where $r_{\mathrm{mi}}$ represents the simulated cumulative precipitation at station $i$, and $r_{\mathrm{oi}}$ denotes the observed precipitation. For MAE, RMSE and sMAPE, values closer to 0 indicate better simulation performance. The aMAPE is used to evaluate whether the simulated precipitation is overestimated or underestimated relative to observations. When aMAPE $> 0$, the precipitation is overestimated; when aMAPE $< 0$, the precipitation is underestimated.

The horizontal hydrometeor fluxes shown in Sect. 3.3 are calculated using a grid-based mass transport formulation. For each model layer, the flux is computed as

$$F = \rho_{\mathrm{air}} q_x V_n \Delta z \Delta s \quad (7)$$

where $F$ is the hydrometeor flux (kg s$^{-1}$), $\rho_{\mathrm{air}}$ is the air density (kg m$^{-3}$), $q_x$ is the mass mixing ratio of the hydrometeor species (kg kg$^{-1}$), $V_n$ is the wind component normal to the cross section (m s$^{-1}$). Specifically, for the north–south cross section along 116° E (33–50° N), $V_n$ is taken as the zonal wind component; for the west–east cross section along 33° N (103–116° E), $V_n$ is taken as the meridional wind component. $\Delta z$ is the layer thickness (m), and $\Delta s$ is the horizontal grid spacing along the cross section (m).

## 3 Results

### 3.1 Ice nuclei

During the DP event, the implemented online aerosol–IN nucleation scheme enables dust aerosols to modify the nucleated IN number concentration. Figure 2a and b show the horizontal distribution of the maximum nucleated IN number

**Table 2.** List of Symbols.

| Symbol | Meaning |
|---|---|
| Paacw | Production rate for accretion of cloud water by averaged snow/graupel (Under subfreezing conditions ($T < 0\,°C$), the collected droplets are typically supercooled and freeze onto the surface of snow or graupel particles. In this case, cloud water is converted into snow or graupel, and latent heat of fusion is released, contributing to local warming. Under above-freezing conditions ($T > 0\,°C$), the accreted droplets do not freeze.) |
| Pcact | Production rate for cloud droplet activation from CCN |
| Pcond | Production rate for condensation rate of water vapour to cloud liquid water |
| Pgacr | Production rate for accretion of rain by graupel |
| Pgaci | Production rate for accretion of cloud ice by graupel |
| Pgaut | Production rate for aggregation form snow to graupel |
| Piacr | Prduction rate for accretions of rain by cloud ice |
| Pidep | Production rate for deposition- sublimation rate of cloud ice |
| Pigen | Production rate for heterogeneous nucleation |
| Pinud | Production rate for deposition/condensation freezing to form cloud ice |
| Pinui | Production rate for immersion freezing of cloud water to form cloud ice |
| Pracs | Production rate for accretions of cloud snow by rain |
| Pracw | Production rate for accretion of cloud water by rain |
| Praci | Production rate for accretion of cloud ice by rain |
| Praut | Production rate for aggregation form cloud water ice to form rain |
| Prevps | Production rate for evaporation/condensation rate of cloud water |
| Prevp | Production rate for evaporation/condensation rate of rain |
| Psacr | Production rate for accretions of rain by cloud snow |
| Psaci | Production rate for accretion of cloud ice by snow |
| Psaut | Production rate for aggregation form cloud ice to snow |
| Pscar | Production rate for accretion of rain by snow |
| Psdep | Production rate for deposition- sublimation rate of cloud snow |

concentration between 4 and 7 km above ground level at DP stations during the time period from 00:00 UTC on 11 April to 00:00 UTC on 15 April 2018 for T_CTL and T_IN, respectively. Figure 2c presents the vertical distribution of DP-event-averaged production rate for Nigen for T_CTL (red line) and T_IN (blue line). Figure 2d presents the vertical distribution of cloud ice mass production rate for heterogeneous ice nucleation for T_CTL and T_IN. Based on the variation characteristics, the vertical layer is divided into three parts: layer A, above 7 km (temperature below −18 °C); layer B, between 4 and 7 km (temperature approximately −18 to −1.5 °C); and layer C, below 4 km (temperature approximately −1.5 to 18 °C).

The online aerosol-IN nucleation scheme can correct the systematic underestimation of IN concentrations. The maximum nucleated IN number concentrations in T_CTL can reach $10^2\,L^{-1}$ in layer B during the DP event (Fig. 2a), showing a relatively uniform horizontal pattern, which is much lower than observed IN concentrations ($10^2$–$10^4\,L^{-1}$) during East Asian dust events (Bi et al., 2019; Tobo et al., 2019; Chen et al., 2021; Hu et al., 2023). For example, Chen et al. (2021) measured immersion-mode INPs at Peking University Atmosphere Environment Monitoring Station during spring 2018–2019 and found that dust periods increased INP concentrations by approximately two orders of magnitude, reaching $10^2\,L^{-1}$ between −15 and −28°. The DP-event-averaged production rate for nucleated IN number concentration ranges 0.005–0.01 $L^{-1}\,s^{-1}$ in layer B (Fig. 2c). In T_CTL, the production rate for nucleated IN number concentration increases with height (Fig. 2c), primarily due to the temperature-dependent nature of the original WDM6 scheme. As a result, cloud ice mass production rate due to heterogeneous ice nucleation peak near the −40 °C level (Fig. 2d). Above this layer, IN concentration continues to increase, but production rate of heterogeneously nucleated cloud ice begins to decline due to limited water vapour (Fig. 2d). In the real atmosphere, the number concentration of effective ice-nucleating particles often reaches a maximum in the mid-troposphere rather than at the highest altitudes (He et al., 2023), suggesting that the continuous increase of IN at higher altitudes in T_CTL may inconsistent with typical observed.

In T_IN, the maximum nucleated IN number concentrations can reach $104\,L^{-1}$ in layer B during the DP event (Fig. 2b), closer to those observed or simulated in other East Asian dust events (Bi et al., 2019; Tobo et al., 2019; Chen et al., 2021; Hu et al., 2023). The DP-event-averaged production rate for nucleated IN number concentration ranges from 0.2 to 3.7 $L^{-1}\,s^{-1}$ in layer B (Fig. 2c), and the cloud ice mass production rate for heterogeneous ice nucleation also peaks in this layer, which is consistent with radar observations and other modelling studies (Haarig et al., 2019; He

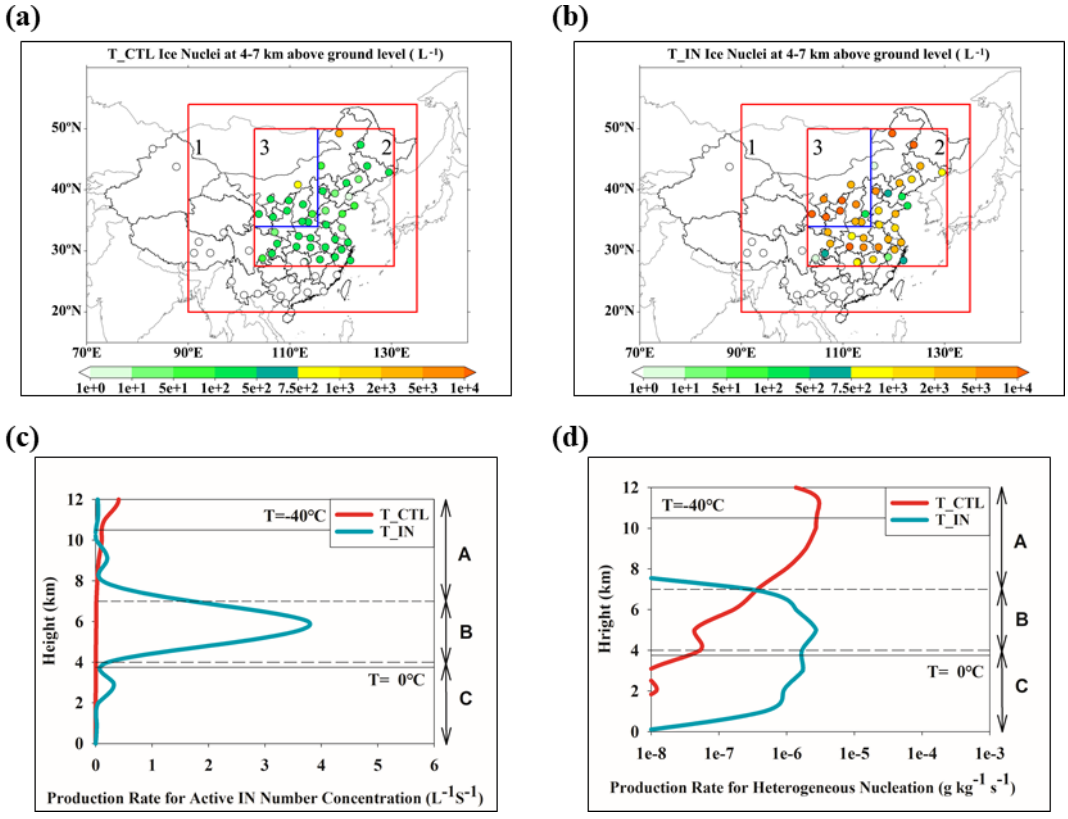


**Figure 2.** Distribution of IN from 11 to 15 April. **(a)** Maximum nucleated IN number concentration at 3–5 km altitude in T_CTL at DP stations; **(b)** Same as **(a)** but for T_IN simulations; **(c)** DP-event-averaged production rate for nucleated IN number concentration for T_CTL (red line) and T_ IN (blue line); **(d)** DP-event-averaged vertical distribution of cloud ice mass production rate for heterogeneous ice nucleation for T_CTL (red line) and T_IN (blue line).

et al., 2021, 2023). As immersion freezing is the dominant heterogeneous nucleation mechanism (DeMott et al., 2015; Hiranuma et al., 2015), this study compares the number concentration of ice-nucleating particles activated by immersion freezing with those activated by deposition and condensation freezing. The DP-event-averaged results indicate that the activated IN number concentration from immersion freezing exceeds that from deposition and condensation freezing by approximately 4–5 orders of magnitude.

## 3.2 Hydrometeors

During the DP event, the introduction of the online aerosol-IN nucleation scheme allows dust aerosols to alter the distribution of cloud hydrometeors. Figure 3 shows the DP-event-averaged vertical distributions of hydrometeors in T_CTL and T_IN, averaged over the dust–precipitation period (00:00 UTC 11 April–00:00 UTC 15 April 2018) and over dust–precipitation stations, as well as their difference (T_IN–T_CTL), by using budget analysis. Figure 4 shows the differences in production rates among hydrometeors (T_IN–T_CTL). To further examine the thermodynamic conditions responsible for the weakened production rate of cloud droplet activation from CCN in T_IN in Fig. 4, the vertical profiles of temperature and water vapour were analyzed, averaged over the dust–precipitation stations in DPA and NDSA during the period when the dust impact was most pronounced (18:00 UTC 11 April to 18:00 UTC 12 April) (Fig. 5).

### 3.2.1 Cloud ice

In layer A, when dust aerosols are considered, the IN number concentration decreases in T_IN (Fig. 2c), resulting in cloud ice number concentrations in T_IN that are approximately 5 $L^{-1}$ lower than those in T_CTL, about 40 % of T_CTL (Fig. 3d). The cloud ice mass concentration is reduced to only 10 %–50 % of T_CTL (Fig. 3a, b). Because the two primary processes contributing to cloud ice formation in this layer—heterogeneous nucleation and deposition-sublimation of cloud ice —are both suppressed (Fig. 4a), and the total production rate of cloud ice (Pigen+Pidep-Psaut-Praci-Psaci-Pgaci) drops to less than 24 % of that in T_CTL. On the one hand, the nucleated IN number concentration decreases, weakening the Pigen in T_IN by 1–2 orders of magnitude relative to T_CTL. On the other hand, the reduction in

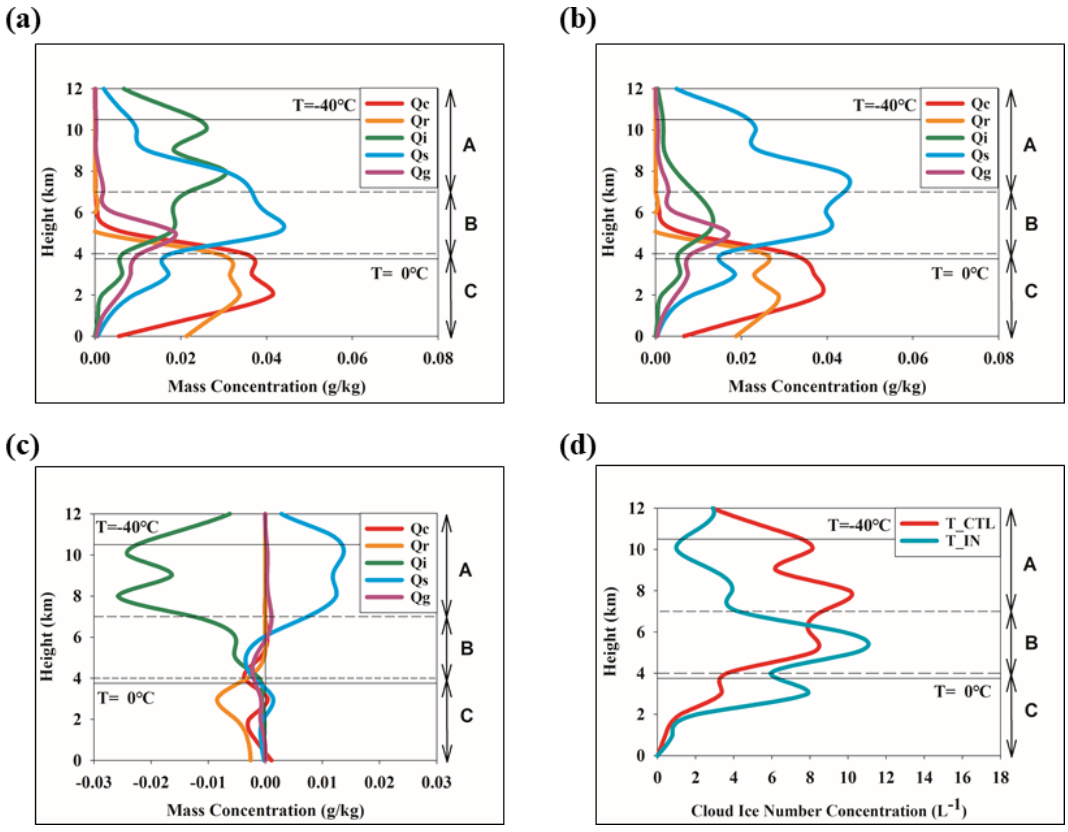


**Figure 3.** Distributions of hydrometeors, averaged over the dust–precipitation period (00:00 UTC 11 April–00:00 UTC 15 April 2018) and over dust–precipitation stations: **(a)** hydrometeors simulated in T_CTL **(b)** hydrometeors simulated in T_IN **(c)** hydrometeors difference by (T_IN- T_CTL); **(d)** DP event-averaged vertical distributions of cloud ice number concentration.

cloud ice number concentration allows ice crystals to grow more efficiently, with their effective particle size generally reaching 98 %–135 % of that in T_CTL. The combined effect of these two factors ultimately limits the deposition of water vapour onto the ice crystals. Consequently, Pidep decreases to 20 %–50 % of T_CTL, with the maximum suppression occurring at approximately 7–8 km (Fig. 4a).

In layer B, cloud ice number concentrations in T_IN range from 7 to 10 $L^{-1}$, approximately 120 % of those in T_CTL. However, the cloud ice mass concentration in T_IN is reduced to only 70 %–90 % of T_CTL. The effective diameters of cloud ice also decrease to only 77 %–97 % of T_CTL, with occasional reductions exceeding 50 %. This reduction is mainly attributable to the combined effects of enhanced heterogeneous nucleation and suppressed depositional growth, and the total production rate of cloud ice drops to less than 82 % of that in T_CTL. Dust aerosols provide additional ice nuclei, leading to a substantial enhancement of heterogeneous nucleation in T_IN and the formation of a much larger number of newly formed small ice crystals, with Pigen exceeding that in T_CTL by more than two orders of magnitude. However, the increase in cloud ice number concentration is accompanied by a reduction in individual particle size, which limits the deposition of water vapour onto ice crystals. This effect is combined with a decrease in relative humidity over dust precipitation stations in the DPA (Fig. 5c), further inhibiting the deposition process. As a result, Pidep in T_IN is reduced to about 30 % of that in T_CTL, indicating that growth of cloud ice via depositional processes is inhibited.

### 3.2.2 Snow

In layer A, the total snow production rate in T_IN increases to approximately 88 %–200 % of that in T_CTL (Psdep+Paacw+Psaut+Piacr+Praci+Psaci+Psacr-Pgaut-Pracs, Fig. 4b), leading to an increase in snow mass concentration to 120 %–200 % of T_CTL (Fig. 3a, b). This increase results from the combined effects of an enhanced production rate for deposition-sublimation of snow (Psdep) and weakened production rates for the aggregation of cloud ice to snow (Psaut) and the accretion of cloud ice by snow (Psaci). The Psdep can reach approximately 2–5 times that in T_CTL (Fig. 4b). In WDM6, the deposition growth of ice-phase hydrometeors is constrained by the available water vapour, with cloud ice deposition given priority and snow deposition consuming the remaining vapour. Because Pidep is reduced to about 20 %–50 % of that in T_CTL,

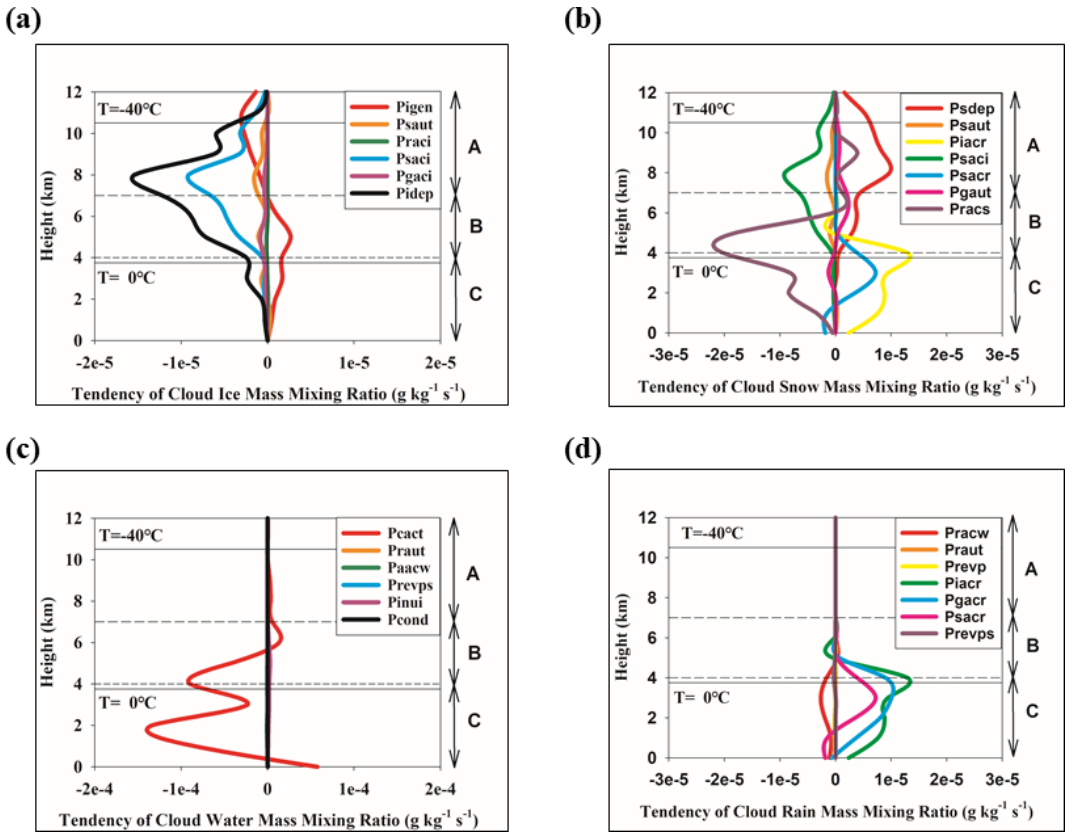


**Figure 4.** Vertical distributions of production rate difference for hydrometeors, averaged over the dust–precipitation period (00:00 UTC 11 April–00:00 UTC 15 April 2018) and over dust–precipitation stations: **(a)** production rate difference for cloud ice **(b)** production rate difference for cloud snow **(c)** production rate difference for cloud water **(d)** production rate difference for cloud rain.

more water vapour is allocated to snow deposition, Psdep is then enhanced. Meanwhile, as cloud ice reduces, Psaut and Psaci are weakened in T_IN, with both processes reduced to approximately 40 %–60 % of their values in T_CTL (Fig. 4a, b). Despite the suppression of these source terms, the substantial enhancement of snow deposition growth dominates the snow budget in layer A, resulting in a net increase in snow production and cloud-snow mass concentration.

Finally, the ratio of cloud ice to cloud snow changes from 1 : 1 to 1 : 3 in layer A, more closely consistent with observation, which shows that cloud ice generally has higher number concentrations but lower mass concentrations than cloud snow (Gao et al., 2020; Yang et al., 2021; Feng et al., 2021). In the aircraft observations reported, small ice particles ($> 50\,\mu m$) reached concentrations of up to $300\,L^{-1}$, whereas large ice crystals ($> 600\,\mu m$) were only about $3\,L^{-1}$ (Wang et al., 2023). Despite their much lower number concentrations, the larger particles contributed more to the ice mass due to their substantially greater size. In the present simulation, the cloud ice number concentrations in T_IN reach on the order of $10^1\,L^{-1}$ in the main mixed-phase layer, which is substantially higher than in T_CTL and closer to the observed magnitudes, although still lower than some aircraft measurements.

In layer B, the snow mass concentration shows relatively small changes, ranging from approximately 90 % to 100 % of T_CTL. From the perspective of cloud microphysics, the mechanisms are similar to those in layer A. Despite the reduction of Pidep, the Psdep increases to 130 %–200 % of T_CTL. At the same time, the decrease in cloud ice mass continues to suppress Psaut and Psaci, resulting in a total snow production rate of about 95 % of T_CTL.

In layer C, although the model diagnostics indicate an enhancement in cloud-snow production processes (production rate for accretion of rain by snow (Psacr) and production rate for accretion of rain by cloud ice (Piacr)) and a reduction in the production rate for accretion of snow by rain (Pracs), newly formed cloud snow cannot be maintained because the temperature is already above 0 °C which makes it instantaneously melt, rapidly converting to rain. As a result, there is no significant change in snow mass concentration in this layer.

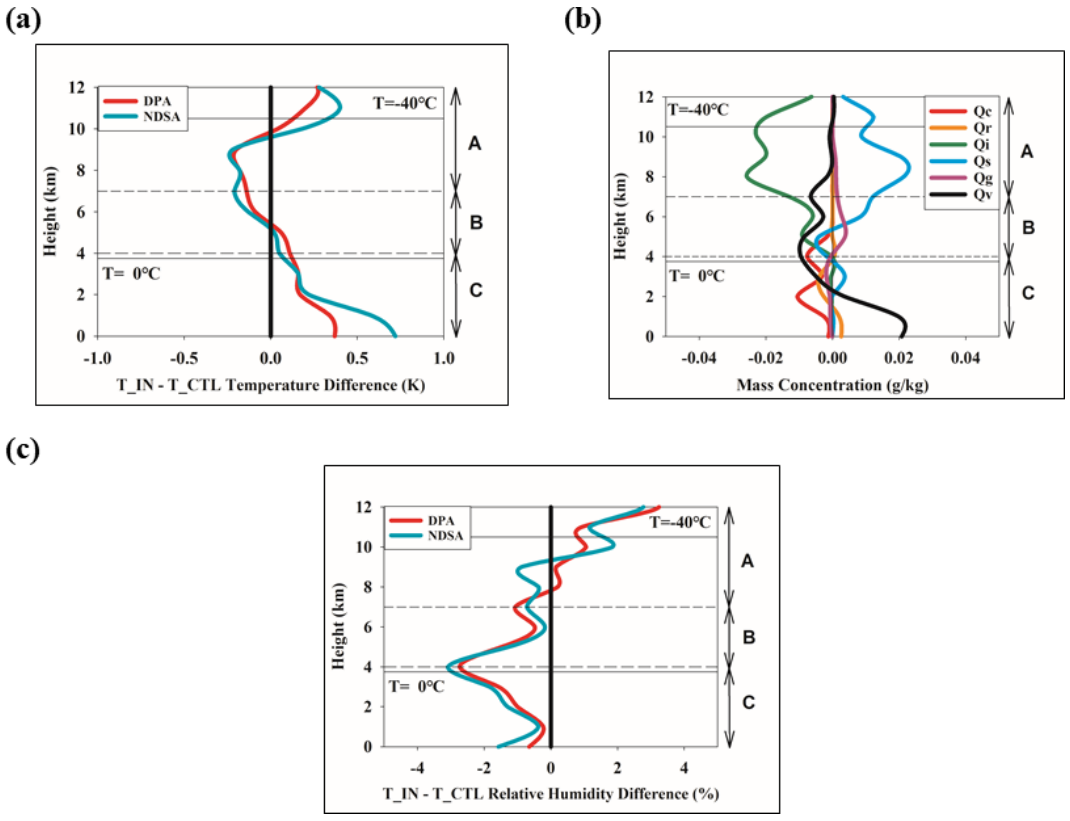


**Figure 5.** Vertical distributions of temperature difference and relative humidity difference, averaged over dust–precipitation stations from 18:00 UTC 11 April to 18:00 UTC 12 April: **(a)** Temperature difference (T_IN-T_CTL) **(b)** Differences in hydrometeor and water vapor mixing ratios (T_IN-T_CTL). For clarity, the water vapor changes are scaled to one-tenth of their actual values. **(c)** Relative humidity difference (T_IN-T_CTL).

### 3.2.3 Cloud water and rainwater

Cloud water and rainwater are mainly distributed in layer C (temperature approximately −2 to 18 °C). In this layer, both cloud-water and rainwater mixing ratios in T_IN are about 90 %–95 % of those in T_CTL. This small reduction is primarily attributed to a weakening of the production rate of cloud droplets via CCN (Pcact), which decreases by about 5 % at T_IN relative to T_CTL, indicating a suppressed conversion of water vapour into liquid water. As a consequence of the reduced cloud-water content, the production rate for accretion of rainwater by cloud water (Pracw) is also weakened by 5 %–10 %. Meanwhile, the conversion of rainwater into ice-phase hydrometeors (Psacr, Pgacr, and Piacr) is enhanced. However, under the thermodynamic conditions of layer C, temperatures exceed the melting thresholds of ice-phase hydrometeors, the newly formed snow and graupel rapidly melt and are easily converted back into rainwater. Consequently, these ice-phase conversion processes contribute only marginally to the net change in rainwater mixing ratio.

Figure 5 shows that, over dust–precipitation stations in both the NDSA and the DPA, the introduction of the online aerosol–IN nucleation scheme leads to temperature increases below 4 km, with changes of about 0.16 to 0.52 K, while the water vapour mixing ratio changes by −0.04 to 0.2 g kg$^{-1}$ during this 18:00 UTC 11 April to 18:00 UTC 12 April. These changes lead to a decrease in relative humidity within the warm-cloud layer. The relative humidity averaged over the dust precipitation stations decreases by up to 3 percentage points during this period in the DPA. In the NDSA, it locally reduces by 6–7 percentage points over a 4 km area at 06:00 UTC 12 April. The reduced relative humidity suppresses droplet activation and condensational growth, thereby inhibiting the development of warm clouds in T_IN compared to T_CTL.

Overall, dust suppresses cloud development, reducing the total ice-phase hydrometeor content in layer A to 70 %–85 % of T_CTL, the total ice-phase hydrometeor content in layer B to 85 %–91 % of T_CTL, and the liquid-phase hydrometeor content in layer C to 90 %–95 % of T_CTL. Our results indicate that dust aerosols tend to suppress cloud development in springtime dust-related precipitation over East Asia, where precipitation is predominantly stratiform. Similar suppression effects have also been reported in previous observational studies (Zhu et al., 2023).

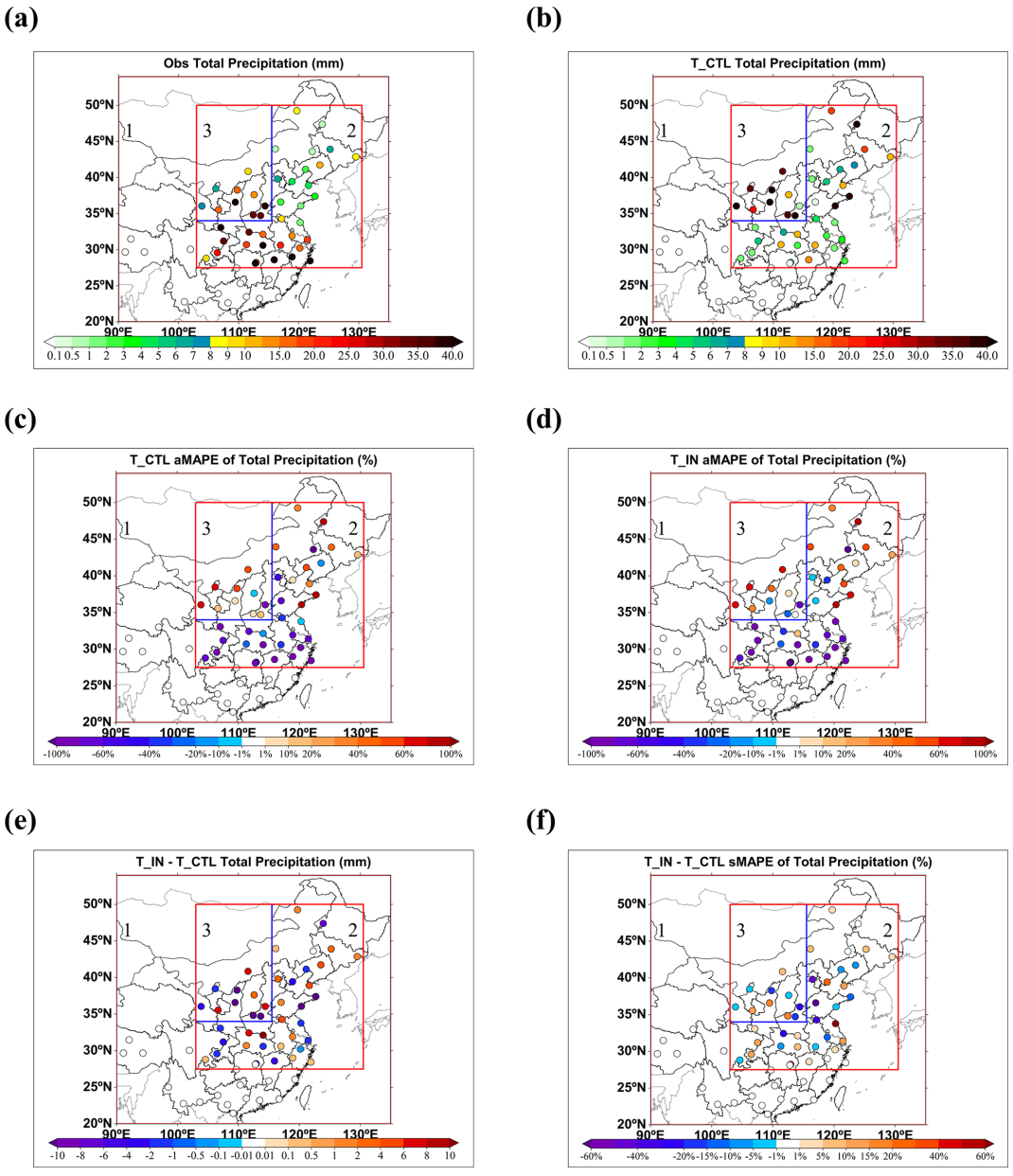


**Figure 6.** Comparison of observed and simulated accumulated precipitation at dust-precipitation stations from 00:00 UTC on 11 April 2018 to 00:00 UTC on 15 April 2018: **(a)** Observed accumulated precipitation; **(b)** Same as in **(a)**, but for T_CTL; **(c)** aMAPE of simulated accumulated precipitation in T_CTL; **(d)** aMAPE of simulated accumulated precipitation in T_IN; **(e)** Difference in accumulated precipitation between T_IN and T_CTL; **(f)** Difference in sMAPE between T_IN and T_CTL.

### 3.3 Precipitation

The online aerosol–IN nucleation scheme can modulate the spatial distribution of precipitation. Figure 6a shows the observed event-accumulated precipitation of DPA stations, and Fig. 6b shows the simulated event-accumulated precipitation of T_CTL. In T_CTL, 18 of 43 stations in DPA exhibit overestimated simulation precipitation compared to observations (overestimated stations), primarily located in areas near dust sources area such as Gansu, Ningxia, Shaanxi, and Inner Mongolia, as well as northeastern provinces including Shandong, Liaoning, Jilin, and Heilongjiang (Fig. 6b). At these overestimated stations, the observed mean accumulated precipitation is 11.49 mm, while the simulated mean accumulated precipitation is 25.55 mm (Fig. 7), with an average sMAPE of 45 %. The other 25 stations show underestimated simulated precipitation compared to observations (underestimated stations), mainly distributed across Hebei, Beijing, Henan, and the Yangtze River Basin downwind area of the dust events (Fig. 6b). At underestimated stations, the ob-

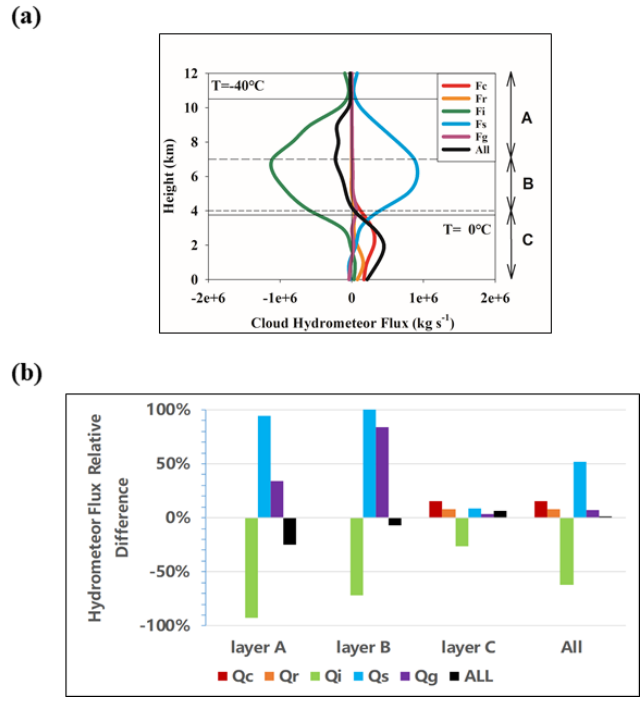


**Figure 7.** Horizontal hydrometeor fluxes across 116° E (33–50° N) and 33° N (103–116° E). Here, Fc denotes cloud water flux, Fr rainwater flux, Fi cloud ice flux, Fs snow flux, Fg graupel flux, and All the total hydrometeor flux. **(a)** Differences in horizontal hydrometeor fluxes (T_IN–T_ CTL). **(b)** Fractional changes in horizontal hydrometeor fluxes in Layers A, B, C, and the total column, defined as (T_IN–T_CTL)/T_CTL. Snow and graupel fluxes in Layer A show extremely large increases (about 1883 % and 683 %, respectively); for better visualization, these values are scaled down by a factor of 20 in the figure.

served mean accumulated precipitation is 31.58 mm (Fig. 7), while the simulated value is only 4.63 mm, with an average sMAPE of −64 %.

In T_IN, the online aerosol–IN nucleation scheme does not alter the overall pattern of overestimation of precipitation north of 35° N and underestimation of precipitation south of 35° N in T_CTL (Fig. 6d). However, compared to T_CTL, notable improvements are mainly observed between 34 and 40° N. This is driven by the process discussed in Sect. 3.2, in which dust in layer C suppresses Pcact, thereby reducing the overestimation of precipitation near dust source areas. sMAPE is reduced by about 1 %–10 % in areas near the dust source, resulting in more accurate forecasts compared to both T_CTL (Fig. 6e, f).

Rather than being removed by precipitation or evaporation, the suppressed cloud hydrometeors are transported downstream in T_IN. We calculate horizontal hydrometeor fluxes across 116° E, 33–50 and 33° N, 103–116° E from 12:00 UTC on 12 April to 18:00 UTC on 13 April (Fig. 7). Over the entire 0–12 km layer, the total hydrometeor flux slightly increases to about 102 % of that in T_CTL.

Within the temperature range from 0 to −40°, the total horizontal hydrometeor flux decreases by about 11 %, primarily due to a substantial reduction in cloud ice flux, accompanied by increases in snow and graupel fluxes. In Layer A, the total hydrometeor flux is about $4.4 \times 10^{-5}$ kg s$^{-1}$, corresponding to about 75 % of T_CTL. Cloud ice flux drops sharply to about 8 % of T_CTL, while snow and graupel fluxes increase markedly to about 19.8 times and 7.8 times, respectively. In Layer B, the total hydrometeor flux is about $2.6 \times 10^{-6}$ kg s$^{-1}$, corresponding to about 93 % of T_CTL, with cloud ice flux reduced to about 28 % of T_CTL, and snow and graupel fluxes increased to about 2.3 times and about 1.8 times, respectively. At temperatures above 0°, the total horizontal hydrometeor flux increases to about 106 % of T_CTL, with cloud water and rainwater fluxes increasing to about 115 % and about 108 %, respectively.

These results indicate that although dust suppresses cold-cloud development in the upper and mid-troposphere, it enhances the downstream transport of liquid-phase hydrometeors near and below the melting layer, enhancing downstream precipitation.

Finally, for underestimation stations, the mean accumulated precipitation increases by 1.1 mm compared to T_CTL, and precipitation simulation improves by approximately 4 %, with little changes in MAE and RMSE (Fig. 8b). For overestimated stations, the mean accumulated precipitation decreases by 4.5 mm compared to T_CTL, and precipitation simulations improves by approximately 40 %, with MAE reduced by 1.4 and RMSE reduced by 4.1 (Fig. 8a).

In summary, because the reduction in cloud water in the 0–4 km layer is relatively small, the corresponding decrease in rainwater reaching the surface is also limited. As a result, the online aerosol–IN nucleation scheme exerts only a weak influence on the total precipitation amount. Nevertheless, it can modulate the spatial and temporal distribution of precipitation, impressing overestimates and altering underestimates to some degree, which is consistent with the findings of Park and Lim (2023) and Su and Fung (2018b).

## 4 Conclusions and discussion

To explore the impact of spring dust aerosols on precipitation, this study develops an online aerosol-IN nucleation scheme within the regional model GRAPES/CUACE. The model performance has been evaluated by a typical dust-precipitation event from 00:00 UTC on 9 April to 00:00 UTC on 15 April 2018.

Dust provides ice nuclei via heterogeneous nucleation during dust precipitation events. The online aerosol–IN nucleation scheme significantly modifies the distributions of nucleated IN concentrations. The original WDM6 scheme exhibits a systematic underestimation of ice-nuclei concentrations, with nucleated IN concentrations reaching $10^2$ L$^{-1}$ between 4 and 7 km altitude during the dust-precipitation event,

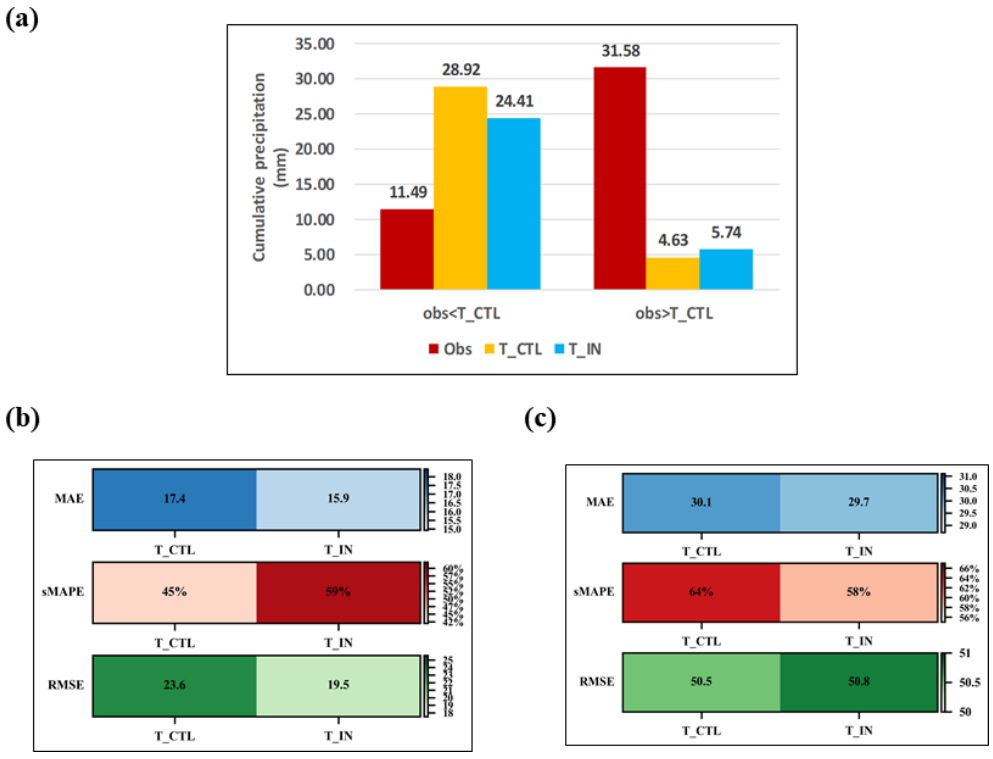


**Figure 8.** **(a)** mean accumulated precipitation during DP event at overestimated stations and underestimated stations **(b)** Statistical analysis of observed versus simulated accumulated precipitation at DPA stations for Overestimated stations **(c)** same as **(b)**, but for Underestimated stations.

and abnormally increasing with height due to its temperature-dependent formulation, peaking near the −40 °C layer. With the online aerosol–IN nucleation scheme, IN concentrations can reach $10^4\ L^{-1}$, so for the cloud ice mass production rate, concentrated peaking at about the layer between 4 and 7 km in height, closer to the observations

Dust can inhibit the development of clouds. Above 7 km, dust suppresses the growth rate of cloud ice (through both heterogeneous nucleation and deposition-sublimation rate of cloud ice), and the total production rate of cloud ice drops to less than 24 % of that in T_CTL, promoting snow formation and ultimately reducing the total ice-phase hydrometeor content to 70 %–85 % of T_CTL. Meanwhile, the total snow production rate in T_IN increases to approximately 88 %–200 % of that in T_CTL, reducing the total ice-phase hydrometeor content to 70 %–85 % of T_CTL. Between 4 and 7 km height, dust enhances heterogeneous nucleation of cloud ice, but the new, smaller particles suppress cloud ice and reduce the deposition rate, resulting in the total ice-phase hydrometeor content decreasing to 85 %–91 % of T_CTL. Below 4 km in height, the relative humidity decreases by about 3 percentage points on average over the dust-precipitation stations in T_IN. This decrease in relative humidity limits the conversion of water vapour to cloud water and of cloud water to rain, reducing the liquid-phase hydrometeor content to 90 %–95 % of that in T_CTL.

The dust can also modulate the spatial distribution of precipitation, even though the online aerosol–IN nucleation scheme cannot fully alter the overall pattern of precipitation overestimation north of 35° N and underestimation south of 35° N, as seen in T_CTL. The online aerosol–IN nucleation scheme mitigates the overestimation of precipitation near dust source areas. For overestimated stations, the event-mean accumulated precipitation decreases by about 4.5 mm relative to T_CTL, with the MAE reducing by 1.4, and the RMSE reducing by 4.1. Meanwhile, the cloud hydrometeors suppressed by dust IN are not removed from the atmosphere; instead, they remain in the weather system and are transported downstream as the air mass moves, thereby alleviating the underestimation of precipitation in downstream areas. In stations where precipitation is previously underestimated, the mean accumulated precipitation increases by about 1.1 mm relative to T_CTL.

This study shows improvements in dust, IN on cloud, and precipitation simulations using a comprehensive online aerosol-IN-cloud interaction scheme. Considering both CCN and IN effects, rather than CCN alone, improves precipitation simulations by up to approximately 40 %. Aerosol-cloud interactions are an old, open question, but many uncertainties remain due to the complex mechanisms of both CCN and IN. Furthermore, the scarcity of real-time observations hinders the in-depth exploration of detailed microphysical processes

and their underlying mechanisms. More cases across different seasons and dust levels are needed in the future, with more observations.

**Code and data availability.** All source code and data can be accessed by contacting the corresponding author, Chunhong Zhou (zhouch@cma.gov.cn) and Xiaoye Zhang (xiaoye@cma.gov.cn).

**Supplement.** The supplement related to this article is available online at https://doi.org/10.5194/acp-26-5407-2026-supplement.

**Author contributions.** JZ developed the online aerosol-IN nucleation scheme, conducted the data analysis, and wrote the original draft of this paper. CHZ developed the aerosol-CCN-cloud interaction scheme and the online aerosol-IN nucleation scheme, and reviewed and edited the manuscript, providing critical insights. XYS reviewed the manuscript. SLG reviewed the manuscript and provided general insight. HW reviewed the manuscript. XYZ reviewed the manuscript and gave guidance on the data analysis. All authors have given approval to the final version of the paper.

**Competing interests.** The contact author has declared that none of the authors has any competing interests.

**Disclaimer.** Publisher's note: Copernicus Publications remains neutral with regard to jurisdictional claims made in the text, published maps, institutional affiliations, or any other geographical representation in this paper. The authors bear the ultimate responsibility for providing appropriate place names. Views expressed in the text are those of the authors and do not necessarily reflect the views of the publisher.

**Acknowledgements.** All figures in this study were produced using the open-source software MeteoInfoLab (http://www.meteothink.org/index.html, last access: 2 April 2026). The meteorological initial and boundary conditions for the modelling system were obtained from the China Meteorological Data Sharing Service System (http://data.cma.cn/data/cdcindex/cid/98c64da7ee348b37html, last access: 2 April 2026). The meteorological observations were obtained from the China Meteorological Data Sharing Service System (http://data.cma.cn/data/cdcindex/cid/f0fb4b55508804ca.html, last access: 2 April 2026). The $PM_{10}$ and $PM_{2.5}$ concentration data were obtained from the national environmental monitoring network of the Ministry of Ecology and Environment of China (http://www.cnemc.cn, last access: 2 April 2026). The NCEP/NCAR Final Operational Global Analysis (FNL) data, with a temporal resolution of 6 h and a spatial resolution of 0.25° (https://rda.ucar.edu/datasets/ds083.3/, last access: 2 April 2026). We are grateful to the two anonymous reviewers for their thoughtful, detailed, constructive comments, which helped to improve the clarity of the paper.

**Financial support.** This study was jointly supported by the NSFC Project (grant no. 42090030), the National Key Project of the Ministry of Science and Technology of China (grant no. 2022YFC3701205), Four-Dimensional Variational Quantitative Inversion of Carbon Dioxide Sources and Sinks in the Ecosystem of the Sichuan Basin (grant no. 2024JDHJ0058), A Study on the Integrated Simulation System for the Interaction Between Greenhouse Gases and Air Quality in Sichuan Province and the Science and Technology Development Fund of CAMS (grant no. 2023KJ003).

**Review statement.** This paper was edited by Hailong Wang and reviewed by two anonymous referees.

## References

Albrecht, B. A.: Aerosols, Cloud Microphysics, and Fractional Cloudiness, Science, 245, 1227–1230, https://doi.org/10.1126/science.245.4923.1227, 1989.

Alfaro, S. and Gomes, L.: Modeling mineral aerosol production by wind erosion: Emission intensities and aerosol size distributions in source areas, J. Geophys. Res., 106, 18075–18084, https://doi.org/10.1029/2000JD900339, 2001.

Andreae, M. O. and Crutzen, P. J.: Atmospheric Aerosols: Biogeochemical Sources and Role in Atmospheric Chemistry, Science, 276, 1052–1058, https://doi.org/10.1126/science.276.5315.1052,1997.

Bi, K., McMeeking, G. R., Ding, D. P., Levin, E. J. T., DeMott, P. J., Zhao, D. L., Wang, F., Liu, Q., Tian, P., Ma, X. C., Chen, Y. B., Huang, M. Y., Zhang, H. L., Gordon, T. D., and Chen, P.: Measurements of Ice Nucleating Particles in Beijing, China, J. Geophys. Res.-Atmos., 124, 8065–8075, https://doi.org/10.1029/2019JD030609, 2019.

Boose, Y., Welti, A., Atkinson, J., Ramelli, F., Danielczok, A., Bingemer, H. G., Plötze, M., Sierau, B., Kanji, Z. A., and Lohmann, U.: Heterogeneous ice nucleation on dust particles sourced from nine deserts worldwide – Part 1: Immersion freezing, Atmos. Chem. Phys., 16, 15075–15095, https://doi.org/10.5194/acp-16-15075-2016, 2016.

Cantrell, W., Bunker, K., Niehaus, J., China, S., Woodward, X., Kostinski, A., and Mazzoleni, C.: Ice nucleation in the contact mode: Temperature and size dependence for selected dusts, AIP Conference Proceedings, 1527, 926, https://doi.org/10.1063/1.4803423, 2013.

Che, Y., Zhang, J., Zhao, C., Fang, W., Xue, W., Yang, W., Ji, D., Dang, J., Duan, J., Sun, J., Shen, X., and Zhou, X.: A study on the characteristics of ice nucleating particles concentration and aerosols and their relationship in spring in Beijing, Atmos. Res., 247, 105196, https://doi.org/10.1016/j.atmosres.2020.105196, 2021.

Chen, D., Xue, J., Yang, X., Zhang, H., Shen, X., Hu, J., Wang, Y., Ji, L., and Chen, J.: New generation of multi-scale NWP system (GRAPES): General scientific design, Chinese Sci. Bull., 53, 3433–3445, https://doi.org/10.1007/s11434-008-0494-z, 2008.

Chen, J., Wu, Z., Chen, J., Reicher, N., Fang, X., Rudich, Y., and Hu, M.: Size-resolved atmospheric ice-nucleating particles during East Asian dust events, Atmos. Chem. Phys., 21, 3491–3506, https://doi.org/10.5194/acp-21-3491-2021, 2021.

Chen, J., Wu, Z., Meng, X., Zhang, C., Chen, J., Qiu, Y., Chen, L., Fang, X., Wang, Y., Zhang, Y., Chen, S., Gao, J., Li, W., and Hu, M.: Observational evidence for the non-suppression effect of atmospheric chemical modification on the ice nucleation activity of East Asian dust, Sci. Total Environ., 861, 160708, https://doi.org/10.1016/j.scitotenv.2022.160708, 2023.

Chen, Q., Yin, Y., Jiang, H., Chu, Z., Xue, L., Shi, R., Zhang, X., and Chen, J.: The Roles of Mineral Dust as Cloud Condensation Nuclei and Ice Nuclei During the Evolution of a Hail Storm, J. Geophys. Res.-Atmos., 124, https://doi.org/10.1029/2019JD031403, 2019.

DeMott, P. J., Prenni, A. J., Liu, X., Kreidenweis, S. M., Petters, M. D., Twohy, C. H., Richardson, M. S., Eidhammer, T., and Rogers, D. C.: Predicting global atmospheric ice nuclei distributions and their impacts on climate, P. Natl. Acad. Sci. USA, 107, 11217–11222, https://doi.org/10.1073/pnas.0910818107, 2010.

DeMott, P. J., Prenni, A. J., McMeeking, G. R., Sullivan, R. C., Petters, M. D., Tobo, Y., Niemand, M., Möhler, O., Snider, J. R., Wang, Z., and Kreidenweis, S. M.: Integrating laboratory and field data to quantify the immersion freezing ice nucleation activity of mineral dust particles, Atmos. Chem. Phys., 15, 393–409, https://doi.org/10.5194/acp-15-393-2015, 2015.

Eastwood, M. L., Cremel, S., Gehrke, C., Girard, E., and Bertram, A. K.: Ice nucleation on mineral dust particles: Onset conditions, nucleation rates and contact angles, J. Geophys. Res.-Atmos., 113, https://doi.org/10.1029/2008JD010639, 2008.

Fan, J., Leung, L. R., DeMott, P. J., Comstock, J. M., Singh, B., Rosenfeld, D., Tomlinson, J. M., White, A., Prather, K. A., Minnis, P., Ayers, J. K., and Min, Q.: Aerosol impacts on California winter clouds and precipitation during CalWater 2011: local pollution versus long-range transported dust, Atmos. Chem. Phys., 14, 81–101, https://doi.org/10.5194/acp-14-81-2014, 2014.

Feng, Q., Niu, S., Hou, T., Fan, X., Shen, D., and Yang, J.: Aircraft – Based Observation of the Physical Characteristics of Snowfall Cloud in Shanxi Province, Chinese J. Atmos. Sci., 45, 1146–1160, https://doi.org/10.3878/j.issn.1006-9895.2106.21004, 2021 (in Chinese).

Filonchyk, M., Yan, H., Shareef, T. M. E., and Yang, S.: Aerosol contamination survey during dust storm process in Northwestern China using ground, satellite observations and atmospheric modeling data, Theor. Appl. Climatol., 135, 119–133, https://doi.org/10.1007/s00704-017-2362-8, 2019.

Gao, Q., Guo, X., He, H., Liu, X., Huang, M., and Ma, X.: Numerical Simulation Study on the Microphysical Characteristics of Stratiform Clouds with Embedded Convections in Northern China based on Aircraft Measurements, Chinese J. Atmos. Sci., 44, 899–912, https://doi.org/10.3878/j.issn.1006-9895.1908.19114, 2020 (in Chinese).

Gibbons, M., Min, Q., and Fan, J.: Investigating the impacts of Saharan dust on tropical deep convection using spectral bin microphysics, Atmos. Chem. Phys., 18, 12161–12184, https://doi.org/10.5194/acp-18-12161-2018, 2018.

Gong, S. L. and Zhang, X. Y.: CUACE/Dust – an integrated system of observation and modeling systems for operational dust forecasting in Asia, Atmos. Chem. Phys., 8, 2333–2340, https://doi.org/10.5194/acp-8-2333-2008, 2008.

Gong, S. L., Zhang, X. Y., Zhao, T. L., McKendry, I. G., Jaffe, D. A., and Lu, N. M.: Characterization of soil dust aerosol in China and its transport and distribution during 2001 ACE-Asia: 2. Model simulation and validation, J. Geophys. Res.-Atmos., 108, https://doi.org/10.1029/2002JD002633, 2003.

Haarig, M., Ansmann, A., Walser, A., Baars, H., Urbanneck, C., Weinzierl, B., Schöberl, M., Dollner, M., Mamouri, R., and Althausen, D.: Estimation of dust related ice nucleating particles in the atmosphere: Comparison of profiling and in-situ measurements, E3S Web Conf., 99, 04002, https://doi.org/10.1051/e3sconf/20199904002, 2019.

Harmoko, I. W., Zainuri, M., Wirasatriya, A., and Supari, S.: Evaluating The Accuracy of Gridded Climate Datasets for Precipitation, Surface Air Temperature, and Sea Surface Temperature in Central Java, Indonesia, Indonesian J. Appl. Phys., 15, 464–476, https://doi.org/10.13057/ijap.v15i2.104276, 2025.

He, C., Yin, Y., Huang, Y., Kuang, X., Cui, Y., Chen, K., Jiang, H., Kiselev, A., Möhler, O., and Schrod, J.: The Vertical Distribution of Ice-Nucleating Particles over the North China Plain: A Case of Cold Front Passage, Remote Sens., 15, 4989, https://doi.org/10.3390/rs15204989, 2023.

He, Y., Zhang, Y., Liu, F., Yin, Z., Yi, Y., Zhan, Y., and Yi, F.: Retrievals of dust-related particle mass and ice-nucleating particle concentration profiles with ground-based polarization lidar and sun photometer over a megacity in central China, Atmos. Meas. Tech., 14, 5939–5954, https://doi.org/10.5194/amt-14-5939-2021, 2021.

Herbert, R. J., Murray, B. J., Dobbie, S. J., and Koop, T.: Sensitivity of liquid clouds to homogenous freezing parameterizations, Geophys. Res. Lett., 42, 1599–1605, https://doi.org/10.1002/2014GL062729, 2015.

Hiranuma, N., Augustin-Bauditz, S., Bingemer, H., Budke, C., Curtius, J., Danielczok, A., Diehl, K., Dreischmeier, K., Ebert, M., Frank, F., Hoffmann, N., Kandler, K., Kiselev, A., Koop, T., Leisner, T., Möhler, O., Nillius, B., Peckhaus, A., Rose, D., Weinbruch, S., Wex, H., Boose, Y., DeMott, P. J., Hader, J. D., Hill, T. C. J., Kanji, Z. A., Kulkarni, G., Levin, E. J. T., McCluskey, C. S., Murakami, M., Murray, B. J., Niedermeier, D., Petters, M. D., O'Sullivan, D., Saito, A., Schill, G. P., Tajiri, T., Tolbert, M. A., Welti, A., Whale, T. F., Wright, T. P., and Yamashita, K.: A comprehensive laboratory study on the immersion freezing behavior of illite NX particles: a comparison of 17 ice nucleation measurement techniques, Atmos. Chem. Phys., 15, 2489–2518, https://doi.org/10.5194/acp-15-2489-2015, 2015.

Hong, S.-Y., Dudhia, J., and Chen, S.-H.: A Revised Approach to Ice Microphysical Processes for the Bulk Parameterization of Clouds and Precipitation, Mon. Weather Rev., 132, 103–120, https://doi.org/10.1175/1520-0493(2004)132<0103:ARATIM>2.0.CO;2, 2004.

Hu, Y., Tian, P., Huang, M., Bi, K., Schneider, J., Umo, N. S., Ullmerich, N., Höhler, K., Jing, X., Xue, H., Ding, D., Liu, Y., Leisner, T., and Möhler, O.: Characteristics of ice-nucleating particles in Beijing during spring: A comparison study of measurements between the suburban and a nearby mountain area, Atmos. Environ., 293, 119451, https://doi.org/10.1016/j.atmosenv.2022.119451, 2023.

Igel, A. L., Igel, M. R., and van den Heever, S. C.: Make It a Double? Sobering Results from Simulations Using Single-Moment Microphysics Schemes, J. Atmos. Sci., 72, 910–925, https://doi.org/10.1175/JAS-D-14-0107.1, 2015.

Ilotoviz, E., Khain, A. P., Benmoshe, N., Phillips, V. T. J., and Ryzhkov, A. V.: Effect of Aerosols on Freezing Drops, Hail, and

Precipitation in a Midlatitude Storm, J. Atmos. Sci., 73, 109–144, https://doi.org/10.1175/JAS-D-14-0155.1, 2016.

Jiang, H., Yin, Y., Su, H., Shan, Y., and Gao, R.: The characteristics of atmospheric ice nuclei measured at the top of Huangshan (the Yellow Mountains) in Southeast China using a newly built static vacuum water vapor diffusion chamber, Atmos. Res., 153, 200–208, https://doi.org/10.1016/j.atmosres.2014.08.015, 2015.

Jiang, H., Yin, Y., Wang, X., Gao, R., Yuan, L., Chen, K., and Shan, Y.: The measurement and parameterization of ice nucleating particles in different backgrounds of China, Atmos. Res., 181, 72–80, https://doi.org/10.1016/j.atmosres.2016.06.013, 2016.

Kang, J.-Y., Yoon, S., Shao, Y., and Kim, S.-W.: Comparison of vertical dust flux by implementing three dust emission schemes in WRF/Chem, J. Geophys. Res., 116, https://doi.org/10.1029/2010JD014649, 2011.

Kang, Y., Jin, S., Peng, X., Yang, X., Shang, K., and Wang, S.: Comparative Analysis of Single-Moment and Double-Moment Microphysics Schemes in WRF on the Torrential Rainfall Event in North China During 1921 July, 2016, Plateau Meteorology, 37, 481–494, 2018.

Kanji, Z. A., Ladino, L. A., Wex, H., Boose, Y., Burkert-Kohn, M., Cziczo, D. J., and Krämer, M.: Overview of Ice Nucleating Particles, Meteorological Monographs, 58, 1.1–1.33, https://doi.org/10.1175/AMSMONOGRAPHS-D-16-0006.1, 2017.

Kaufman, Y. J., Tanré, D., and Boucher, O.: A satellite view of aerosols in the climate system, Nature, 419, 215–223, https://doi.org/10.1038/nature01091, 2002.

Khain, A., Ovtchinnikov, M., Pinsky, M., Pokrovsky, A., and Krugliak, H.: Notes on the state-of-the-art numerical modeling of cloud microphysics, Atmos. Res., 55, 159–224, https://doi.org/10.1016/S0169-8095(00)00064-8, 2000.

Knopf, D. A. and Alpert, P. A.: Atmospheric ice nucleation, Nat. Rev. Phys., 5, 203–217, https://doi.org/10.1038/s42254-023-00570-7, 2023.

Kumar, V. A., Pandithurai, G., Kulkarni, G., Hazra, A., Patil, S. S., Dudhambe, S. D., Patil, R. D., Chen, J.-P., and Niranjan, K.: Atmospheric ice nuclei concentration measurements over a high altitude-station in the Western Ghats, India, Atmos. Res., 235, 104795, https://doi.org/10.1016/j.atmosres.2019.104795, 2020.

Lee, S. S., Kim, B.-G., Yum, S. S., Seo, K.-H., Jung, C.-H., Um, J. S., Li, Z., Hong, J., Chang, K.-H., and Jeong, J.-Y.: Effects of aerosol on evaporation, freezing and precipitation in a multiple cloud system, Clim. Dynam., 48, 1069–1087, https://doi.org/10.1007/s00382-016-3128-1, 2017.

Li, J., Liu, W., Castarède, D., Gu, W., Li, L., Ohigashi, T., Zhang, G., Tang, M., Thomson, E. S., Hallquist, M., Wang, S., and Kong, X.: Hygroscopicity and Ice Nucleation Properties of Dust/Salt Mixtures Originating from the Source of East Asian Dust Storms, Front. Environ. Sci., 10, https://doi.org/10.3389/fenvs.2022.897127, 2022.

Li, M., Zhang, Q., Kurokawa, J.-I., Woo, J.-H., He, K., Lu, Z., Ohara, T., Song, Y., Streets, D. G., Carmichael, G. R., Cheng, Y., Hong, C., Huo, H., Jiang, X., Kang, S., Liu, F., Su, H., and Zheng, B.: MIX: a mosaic Asian anthropogenic emission inventory under the international collaboration framework of the MICS-Asia and HTAP, Atmos. Chem. Phys., 17, 935–963, https://doi.org/10.5194/acp-17-935-2017, 2017.

Liu, H., Yu, Y., Xia, D., Zhao, S., Ma, X., and Dong, L.: Analysis of the relationship between dust aerosol and precipitation in spring over East Asia using EOF and SVD methods, Sci. Total Environ., 908, 168437, https://doi.org/10.1016/j.scitotenv.2023.168437, 2024.

Marticorena, B. and Bergametti, G.: Modeling the atmospheric dust cycle: 1. Design of a soil-derived dust emission scheme, J. Geophys. Res.-Atmos., 100, 16415–16430, https://doi.org/10.1029/95JD00690, 1995.

Mascioli, N. R., Evan, A. T., and Ralph, F. M.: Influence of Dust on Precipitation During Landfalling Atmospheric Rivers in an Idealized Framework, J. Geophys. Res.-Atmos., 126, e2021JD034813, https://doi.org/10.1029/2021JD034813, 2021.

Molthan, A. L. and Colle, B. A.: Comparisons of Single- and Double-Moment Microphysics Schemes in the Simulation of a Synoptic-Scale Snowfall Event, Mon. Weather Rev., 140, 2982–3002, https://doi.org/10.1175/MWR-D-11-00292.1, 2012.

Naeger, A. R.: Impact of dust aerosols on precipitation associated with atmospheric rivers using WRF-Chem simulations, Result. Phys., 10, 217–221, https://doi.org/10.1016/j.rinp.2018.05.027, 2018.

Nenes, A., Murray, B., and Bougiatioti, A.: Mineral Dust and its Microphysical Interactions with Clouds, Mineral Dust: A Key Player in the Earth System, 287–325, https://doi.org/10.1007/978-94-017-8978-3_12, 2014.

Niehaus, J., Becker, J. G., Kostinski, A., and Cantrell, W.: Laboratory Measurements of Contact Freezing by Dust and Bacteria at Temperatures of Mixed-Phase Clouds, J. Atmos. Sci., 71, 3659–3667, https://doi.org/10.1175/JAS-D-14-0022.1, 2014.

Pan, X., Uno, I., Wang, Z., Nishizawa, T., Sugimoto, N., Yamamoto, S., Kobayashi, H., Sun, Y., Fu, P., Tang, X., and Wang, Z.: Real-time observational evidence of changing Asian dust morphology with the mixing of heavy anthropogenic pollution, Sci. Rep., 7, 335, https://doi.org/10.1038/s41598-017-00444-w, 2017.

Park, S.-Y. and Lim, K.-S. S.: Implementation of Prognostic Cloud Ice Number Concentrations for the Weather Research and Forecasting (WRF) Double-Moment 6-Class (WDM6) Microphysics Scheme, J. Adv. Model. Earth Syst., 15, e2022MS003009, https://doi.org/10.1029/2022MS003009, 2023.

Patnaude, R. J., McCluskey, C. S., Roberts, G. C., DeMott, P. J., Hill, T. C. J., McFarquhar, G. M., Kollias, P., Ranjbar, K., Wolde, M., and Kreidenweis, S. M.: Characteristics of Ice Nucleating Particles From the Long-Range Transport of Saharan Dust, Geophys. Res. Lett., 52, e2024GL113365, https://doi.org/10.1029/2024GL113365, 2025.

Possner, A., Ekman, A. M. L., and Lohmann, U.: Cloud response and feedback processes in stratiform mixed-phase clouds perturbed by ship exhaust, Geophys. Res. Lett., 44, 1964–1972, https://doi.org/10.1002/2016GL071358, 2017.

Pu, Z. and Lin, C.: Evaluation of double-moment representation of ice hydrometeors in bulk microphysical parameterization: comparison between WRF numerical simulations and UND-Citation data during MC3E, Geosci. Lett., 2, 11, https://doi.org/10.1186/s40562-015-0028-x, 2015.

Shao, Y., Ishizuka, M., Mikami, M., and Leys, J. F.: Parameterization of size-resolved dust emission and validation with measurements, J. Geophys. Res.-Atmospheres, 116, https://doi.org/10.1029/2010JD014527, 2011.

Shen, X., Shi, Y., Wang, H., Zhang, M., and Han, J.: Comparison of two double-moment cloud microphysics schemes in the GRAPES_Meso model on simulating a cold cloud process, Torrential Rain Disaster., 41, 336–347, https://doi.org/10.3969/j.issn.1004-9045.2022.03.010, 2022.

Shen, X., Mei, H., Wang, W., and Huang, W.: Numerical Simulation of Ice-Phase Processes Using a Double-Moment Microphysical Scheme and a Sensitivity Test of Ice Nuclei Concentration, Chinese J. Atmos. Sci., 39, 83–99, https://doi.org/10.3878/j.issn.1006-9895.1405.13310, 2024.

Stevens, R. G., Loewe, K., Dearden, C., Dimitrelos, A., Possner, A., Eirund, G. K., Raatikainen, T., Hill, A. A., Shipway, B. J., Wilkinson, J., Romakkaniemi, S., Tonttila, J., Laaksonen, A., Korhonen, H., Connolly, P., Lohmann, U., Hoose, C., Ekman, A. M. L., Carslaw, K. S., and Field, P. R.: A model intercomparison of CCN-limited tenuous clouds in the high Arctic, Atmos. Chem. Phys., 18, 11041–11071, https://doi.org/10.5194/acp-18-11041-2018, 2018.

Stier, P., van den Heever, S. C., Christensen, M. W., Gryspeerdt, E., Dagan, G., Saleeby, S. M., Bollasina, M., Donner, L., Emanuel, K., Ekman, A. M. L., Feingold, G., Field, P., Forster, P., Haywood, J., Kahn, R., Koren, I., Kummerow, C., L'Ecuyer, T., Lohmann, U., Ming, Y., Myhre, G., Quaas, J., Rosenfeld, D., Samset, B., Seifert, A., Stephens, G., and Tao, W.-K.: Multifaceted aerosol effects on precipitation, Nat. Geosci., 17, 719–732, https://doi.org/10.1038/s41561-024-01482-6, 2024.

Stith, J. L., Ramanathan, V., Cooper, W. A., Roberts, G. C., DeMott, P. J., Carmichael, G., Hatch, C. D., Adhikary, B., Twohy, C. H., Rogers, D. C., Baumgardner, D., Prenni, A. J., Campos, T., Gao, R., Anderson, J., and Feng, Y.: An overview of aircraft observations from the Pacific Dust Experiment campaign, J. Geophys. Res.-Atmos., 114, https://doi.org/10.1029/2008JD010924, 2009.

Su, L. and Fung, J. C. H.: Investigating the role of dust in ice nucleation within clouds and further effects on the regional weather system over East Asia – Part 1: model development and validation, Atmos. Chem. Phys., 18, 8707–8725, https://doi.org/10.5194/acp-18-8707-2018, 2018a.

Su, L. and Fung, J. C. H.: Investigating the role of dust in ice nucleation within clouds and further effects on the regional weather system over East Asia – Part 2: modification of the weather system, Atmos. Chem. Phys., 18, 11529–11545, https://doi.org/10.5194/acp-18-11529-2018, 2018b.

Tobo, Y., Adachi, K., DeMott, P. J., Hill, T. C. J., Hamilton, D. S., Mahowald, N. M., Nagatsuka, N., Ohata, S., Uetake, J., Kondo, Y., and Koike, M.: Glacially sourced dust as a potentially significant source of ice nucleating particles, Nat. Geosci., 12, 253–258, https://doi.org/10.1038/s41561-019-0314-x, 2019.

Tobo, Y., Uetake, J., Matsui, H., Moteki, N., Uji, Y., Iwamoto, Y., Miura, K., and Misumi, R.: Seasonal Trends of Atmospheric Ice Nucleating Particles Over Tokyo, J. Geophys. Res.-Atmos., 125, e2020JD033658, https://doi.org/10.1029/2020JD033658, 2020.

Trochkine, D., Iwasaka, Y., Matsuki, A., Yamada, M., Kim, Y.-S., Nagatani, T., Zhang, D., Shi, G.-Y., and Shen, Z.: Mineral aerosol particles collected in Dunhuang, China, and their comparison with chemically modified particles collected over Japan, J. Geophys. Res.-Atmos., 108, https://doi.org/10.1029/2002JD003268, 2003.

Um, J., McFarquhar, G. M., Stith, J. L., Jung, C. H., Lee, S. S., Lee, J. Y., Shin, Y., Lee, Y. G., Yang, Y. I., Yum, S. S., Kim, B.-G., Cha, J. W., and Ko, A.-R.: Microphysical characteristics of frozen droplet aggregates from deep convective clouds, Atmos. Chem. Phys., 18, 16915–16930, https://doi.org/10.5194/acp-18-16915-2018, 2018.

Wang, H., Gong, S. L., Zhang, H. L., Chen, Y., Shen, X. S., Chen, D. H., Xue, J. S., Shen, Y. F., and Jin, W. Z.: A new-generation sand and dust storm forecasting system GRAPES_CUACE/Dust: Model development, verification and numerical simulation, Chinese Sci. Bull., https://doi.org/10.1007/s11434-009-0481-z, 2010.

Wang, H., Zhang, X. Y., Wang, P., Peng, Y., Zhang, W. J., Liu, Z. D., Han, C., Li, S. T., Wang, Y. Q., Che, H. Z., Huang, L. P., Liu, H. L., Zhang, L., Zhou, C. H., Ma, Z. S., Chen, F. F., Ma, X., Wu, X. J., Zhang, B. H., and Shen, X. S.: Chemistry-Weather Interacted Model System GRAPES_Meso5.1/CUACE CW V1.0: Development, Evaluation and Application in Better Haze/Fog Prediction in China, J. Adv. Model. Earth Syst., 14, e2022MS003222, https://doi.org/10.1029/2022MS003222, 2022.

Wang, J., Wang, T., Yasheng, D., Wang, X., Lei, Y., Li, X., Wang, Z., and Shi, B.: Modulations of dust aerosols on precipitation: Evidence from a typical heavy sandstorm event, Atmos. Res., 304, 107411, https://doi.org/10.1016/j.atmosres.2024.107411, 2024.

Wang, W., Sheng, L., Jin, H., and Han, Y.: Dust aerosol effects on cirrus and altocumulus clouds in Northwest China, J. Meteorol. Res., 29, 793–805, https://doi.org/10.1007/s13351-015-4116-9, 2015.

Wang, Y. and Yan, Z.: Effect of Different Verification Schemes on Precipitation Verification and Assessment Conclusion, Meteorol. Month., 33, 53–61, https://doi.org/10.3969/j.issn.1000-0526.2007.12.008, 2007.

Wang, Y., Kong, R., Cai, M., Zhou, Y., Song, C., Liu, S., Li, Q., Chen, H., and Zhao, C.: High small ice concentration in stratiform clouds over Eastern China based on aircraft observations: Habit properties and potential roles of secondary ice production, Atmos. Res., 281, 106495, https://doi.org/10.1016/j.atmosres.2022.106495, 2023.

Xu, G. Q., Chen, D. H., Xue, J. S., Sun, J., and Wang, S. Y.: The program structure designing and optimizing tests of GRAPES physics, Chinese Sci. Bull., 53, 7, https://doi.org/10.1007/s11434-008-0418-y, 2008.

Yang, J., Hu, X., Lei, H., Duan, Y., Lv, F., and Zhao, L.: Airborne Observations of Microphysical Characteristics of Stratiform Cloud Over Eastern Side of Taihang Mountains, Chinese J. Atmos. Sci., 45, 88–106, 2021.

Yang, L., Yin, Y., Yang, S., Jiang, H., Xiao, H., Chen, Q., Su, H., and Chen, C.: Measurement and Analysis of Atmospheric Ice Nuclei in Nanjing, CJAS, 37, 579–594, https://doi.org/10.3878/j.issn.1006-9895.2012.11242, 2013.

Zhang, M., Yu, H., Guo, J., Shen, X., Su, Y., Xue, H., and Dou, B.: Assessment on Unsystematic Errors of GRAPES_GFS 2.0, J. Appl. Meteorol. Sci., 30, 332–344, 2019.

Zhang, W., Wang, H., Zhang, X., Huang, L., Peng, Y., Liu, Z., Zhang, X., and Che, H.: Aerosol–cloud interaction in the atmospheric chemistry model GRAPES_Meso5.1/CUACE and its impacts on mesoscale numerical weather prediction under haze pollution conditions in Jing–Jin–Ji in China, Atmos. Chem. Phys., 22, 15207–15221, https://doi.org/10.5194/acp-22-15207-2022, 2022.

Zhang, Z. and Shen, X.: On the development of the GRAPES – A new generation of the national operational NWP system in China, Chinese Sci. Bull., 53, 4, https://doi.org/10.1007/s11434-008-0462-7, 2008.

Zhao, X., Lin, Y., Luo, Y., Qian, Q., Liu, X., Liu, X., and Colle, B. A.: A Double-Moment SBU-YLIN Cloud Microphysics Scheme and Its Impact on a Squall Line Simulation, J. Adv. Model. Earth Syst., 13, e2021MS002545, https://doi.org/10.1029/2021MS002545, 2021.

Zhou, C., Gong, S., Zhang, X., Liu, H., Xue, M., Cao, G., An, X., Che, H., Zhang, Y., and Niu, T.: Towards the improvements of simulating the chemical and optical properties of Chinese aerosols using an online coupled model – CUACE/Aero, Tellus B, 64, 18965, https://doi.org/10.3402/tellusb.v64i0.18965, 2012.

Zhou, C., Zhang, X., Gong, S., Wang, Y., and Xue, M.: Improving aerosol interaction with clouds and precipitation in a regional chemical weather modeling system, Atmos. Chem. Phys., 16, 145–160, https://doi.org/10.5194/acp-16-145-2016, 2016.

Zhou, C., Gui, H., Hu, J., Ke, H., Wang, Y., and Zhang, X.: Detection of New Dust Sources in Central/East Asia and Their Impact on Simulations of a Severe Sand and Dust Storm, J. Geophys. Res.-Atmos., 124, 10232–10247, https://doi.org/10.1029/2019JD030753, 2019.

Zhou, C., Rao, X., Sheng, L., Zhang, J., Lu, Lin, J., Hu, J., Zhang, B., and Xu, R.: Application of Scale-adaptive Dust Emission Scheme to CMA-CUACE/Dust, J. Appl. Meteor. Sci., 35, 400–413, https://doi.org/10.11898/1001-7313.20240402, 2024.

Zhou, C. H., Gong, S. L., Zhang, X. Y., Wang, Y. Q., Niu, T., Liu, H. L., Zhao, T. L., Yang, Y. Q., and Hou, Q.: Development and evaluation of an operational SDS forecasting system for East Asia: CUACE/Dust, Atmos. Chem. Phys., 8, 787–798, https://doi.org/10.5194/acp-8-787-2008, 2008.

Zhu, H., Li, R., Yang, S., Zhao, C., Jiang, Z., and Huang, C.: The impacts of dust aerosol and convective available potential energy on precipitation vertical structure in southeastern China as seen from multisource observations, Atmos. Chem. Phys., 23, 2421–2437, https://doi.org/10.5194/acp-23-2421-2023, 2023.